Nonlinear III-posed Inverse Problem in X-ray CT

Low-dose Dental Cone Beam Computed Tomography

Tomographic Inverse Problems: Mathematical Challenges and Novel Applications

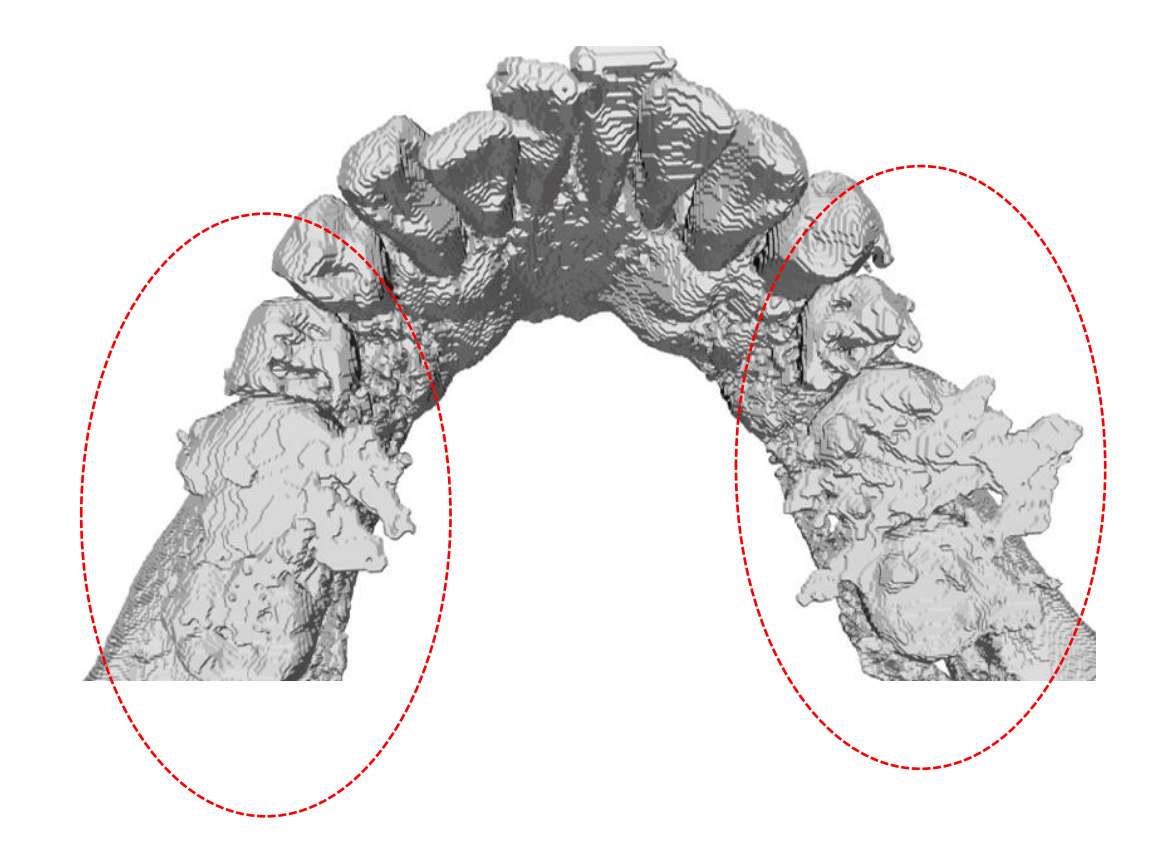
3 May, 2023

Mathematisches Forschungsinstitut Oberwolfach

Jin Keun Seo (Yonsei university, Korea)







Commercial dental CBCTs

- Commercial dental CBCT systems typically utilize a small flat panel detector, which generates a polychromatic and truncated sinogram. Although some manufacturers may advertise the use of photon counting detectors, these features are not widely adopted in dental CBCT practice.
- I try to provide clear explanations of the complex issues involved in commercial dental CBCT imaging, specifically addressing shortcomings in existing methods.





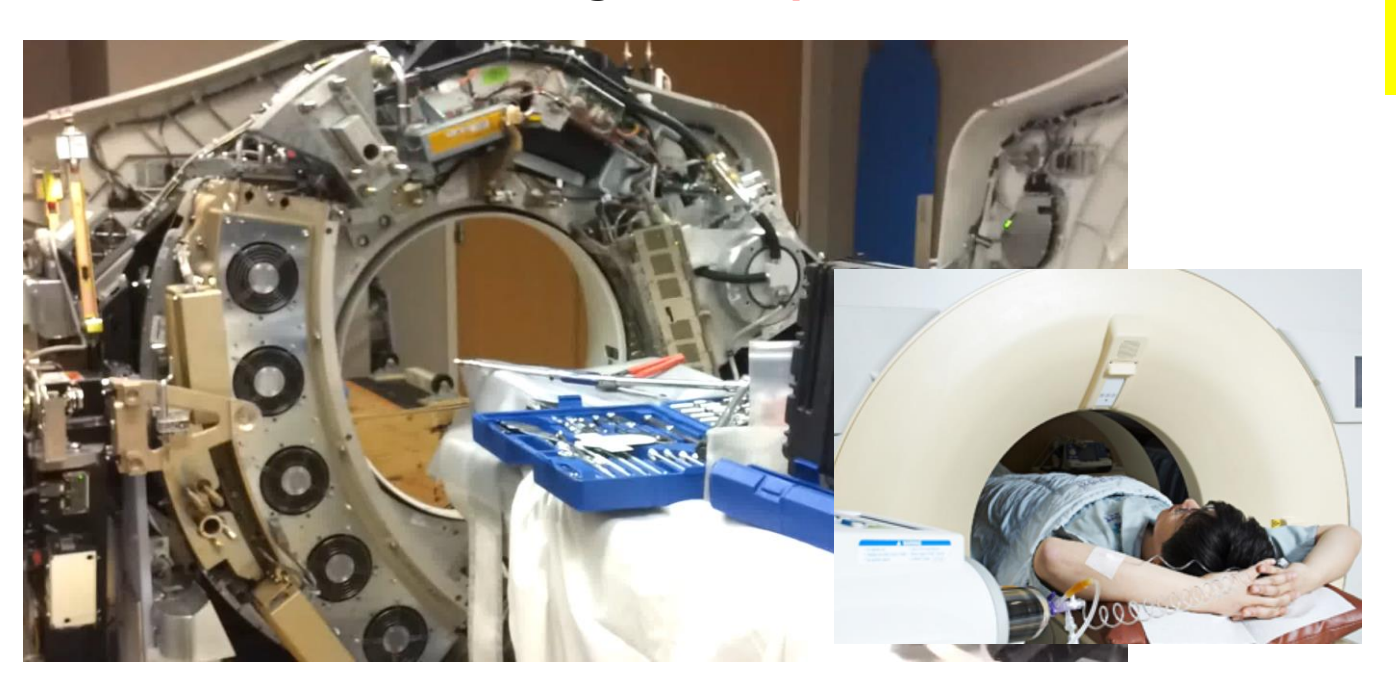




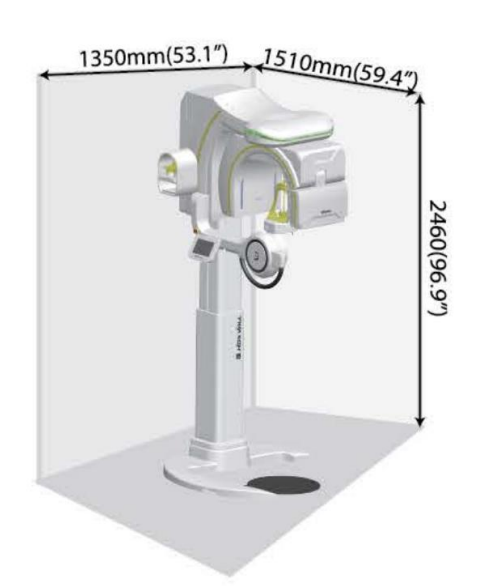


Structural difference between Conventional CT & dental CBCT

The difference is related to the rotation speed of the CT gantry, where stability must be ensured during continuous rotation at high **centripetal forces**.



Most dental CBCT equipment allows the patient to scan while sitting or standing, requiring less space in the dental office. Due to the centripetal force, the scanner gantry cannot be rotated quickly.







- Helical fan-beam
- Scan time per revolution < 0.5s
- Price > \$ 1 million
- Expensive maintenance

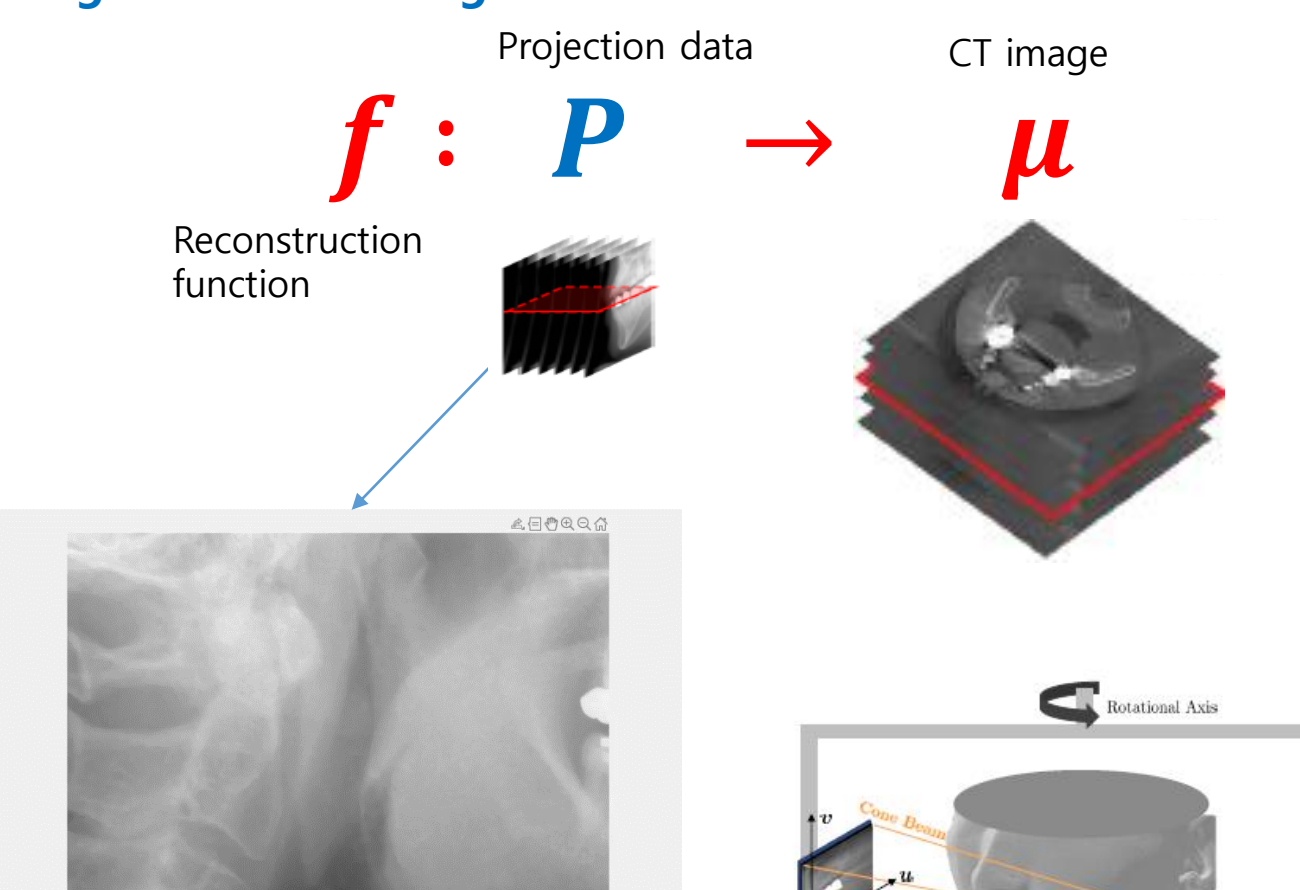


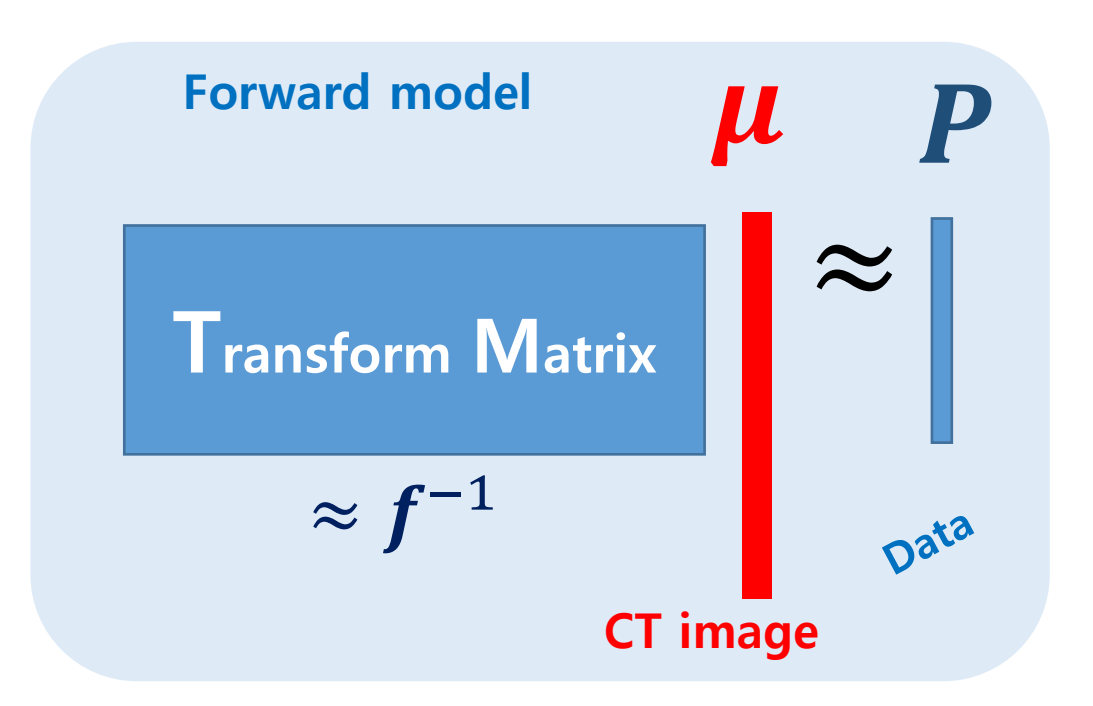
- Circular cone-beam
- Scan time: 8-24sec
- Price < \$ 0.05 million
- Cheap maintenance

Inverse Problem in low-dose dental CBCT

X-ray Tube

The goal is to find a good CT-reconstruction function:



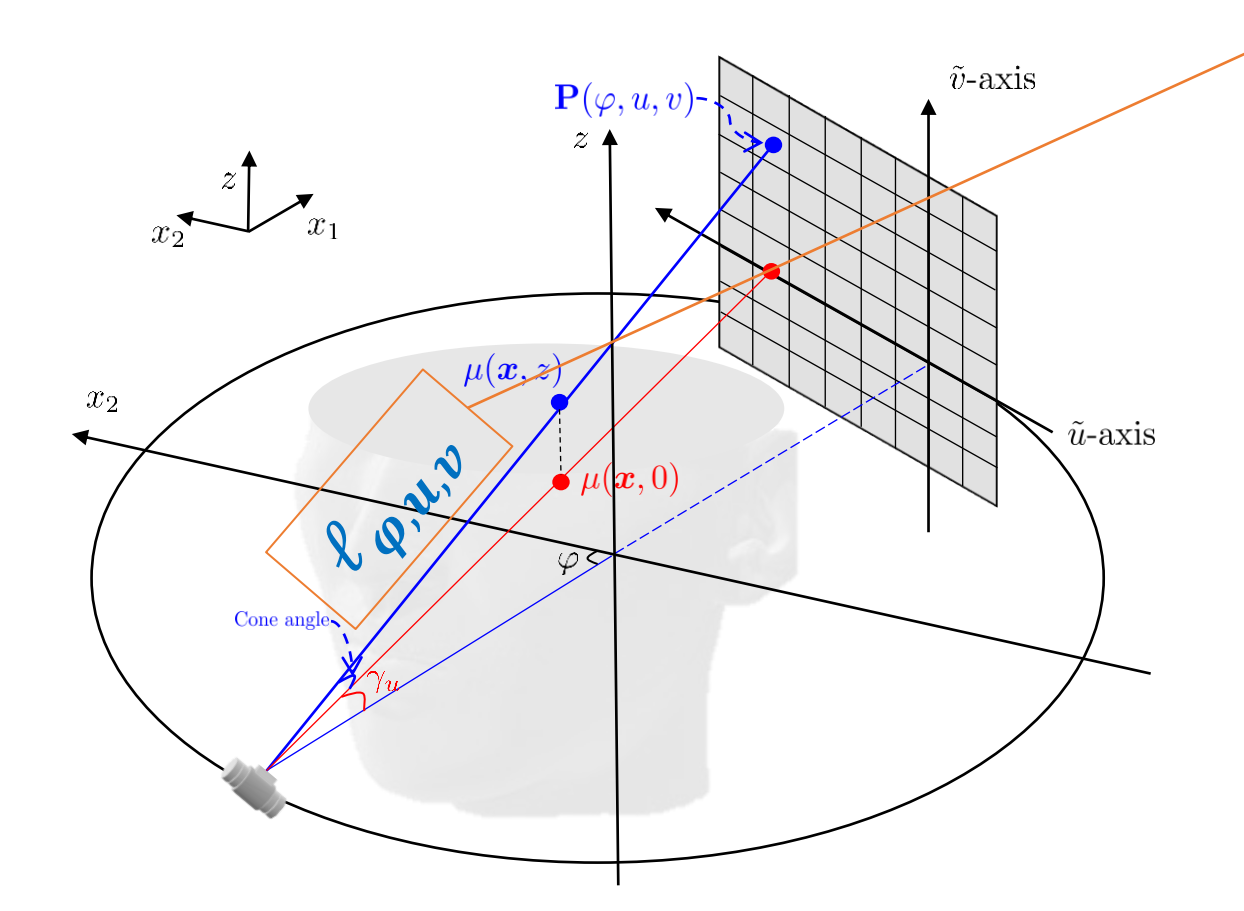


The mathematical model of dental CBCT

Projection Data: Beer-Lambert law

The energy distribution $\eta(E)$ can include photons with energies ranging from 0 keV up to 120 keV.

$$P(\varphi, u, v) = -\ln \int \eta(E) \exp \left(-\int_{\ell_{\varphi,u,v}} \mu_{E}(x, y, z) ds\right) dE$$



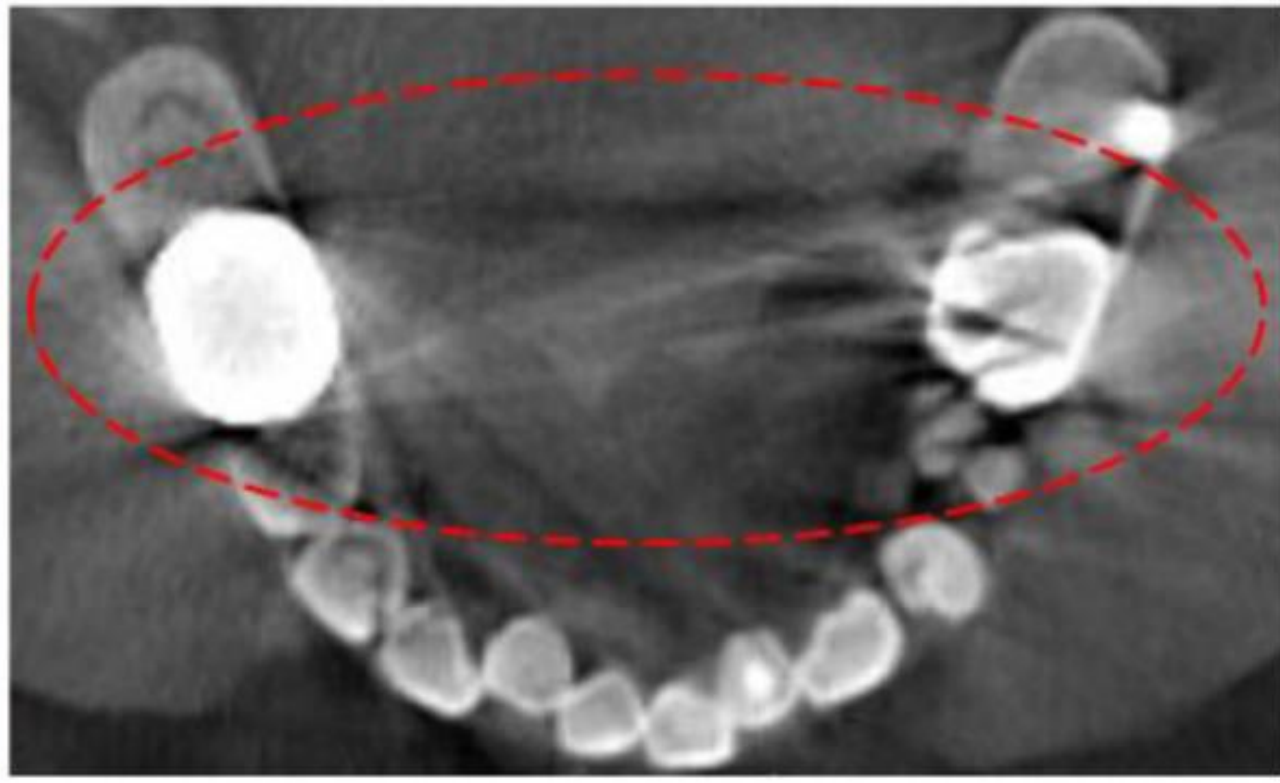
Inverse Problem:

Reconstruct the CT image $\mu = \mu_{E_0}$ (i.e., the tissue density at a fixed energy E_0) from measured projection data P.

FDK (Feldkamp-Davis-Kress) algorithm is a modified version of the inverse Radon transform that is specifically designed for CBCT imaging.

$$\mu(\mathbf{x}, \mathbf{z}) = \mathcal{C}_{\text{FDK}}^{\dagger}[P](\mathbf{x}, z) = \frac{1}{4\pi} \int_{0}^{2\pi} \frac{r^{2}}{U_{\varphi, \mathbf{x}}^{2}} \int P(\varphi, u, \frac{zr}{U_{\varphi, \mathbf{x}}}) \frac{r \, \hbar(r \frac{\mathbf{x} \cdot \Theta_{\varphi}}{U_{\varphi, \mathbf{x}}} - u)}{\sqrt{r^{2} + u^{2} + (\frac{zr}{U_{\varphi, \mathbf{x}}})^{2}}} du d\varphi$$

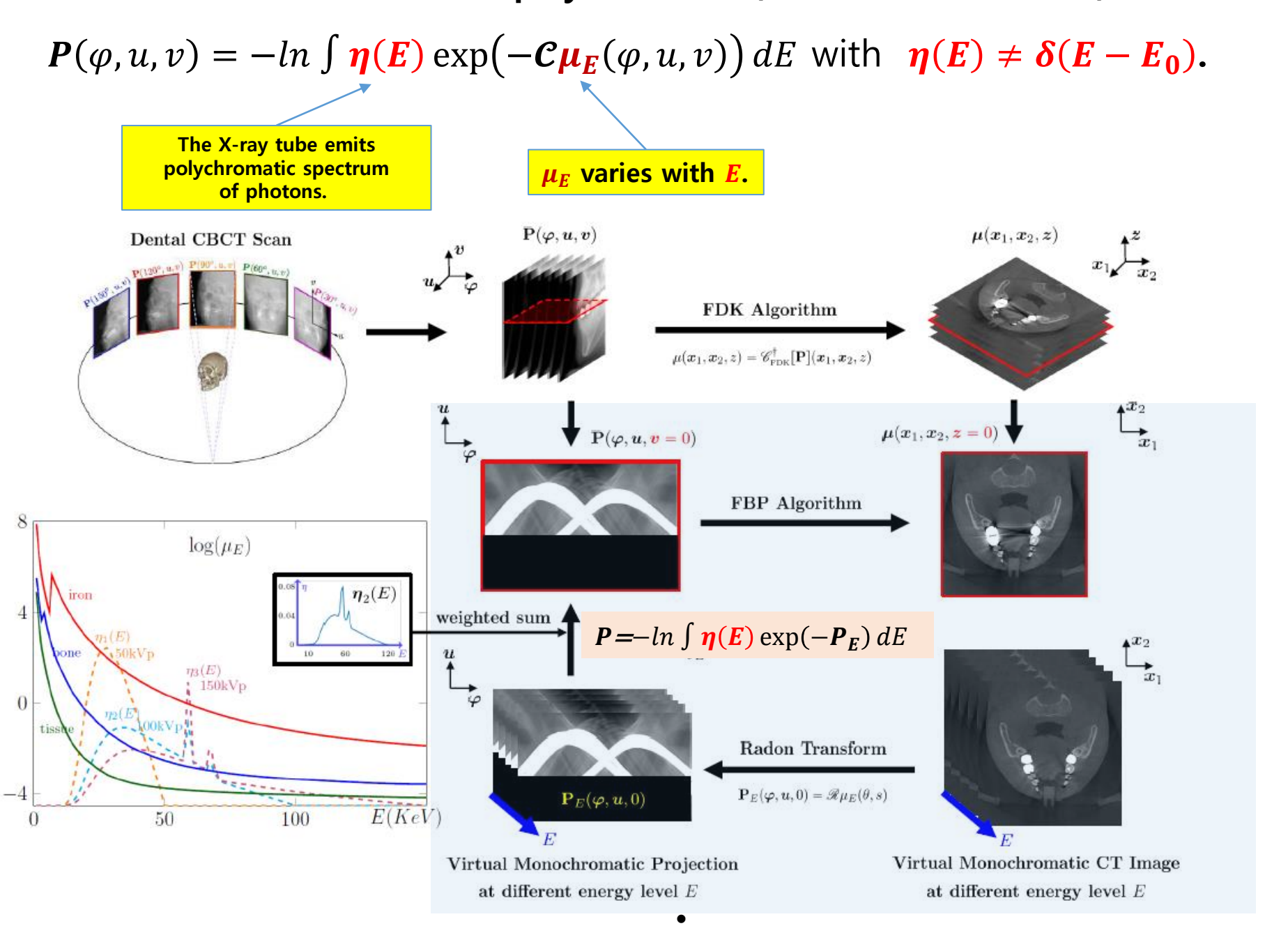




Dental CBCT is a powerful imaging modality that can provide high-quality, three-dimensional images of the teeth, jawbones, and surrounding tissues. However, the presence of metal implants can cause significant image artifacts and reduce the overall image quality.

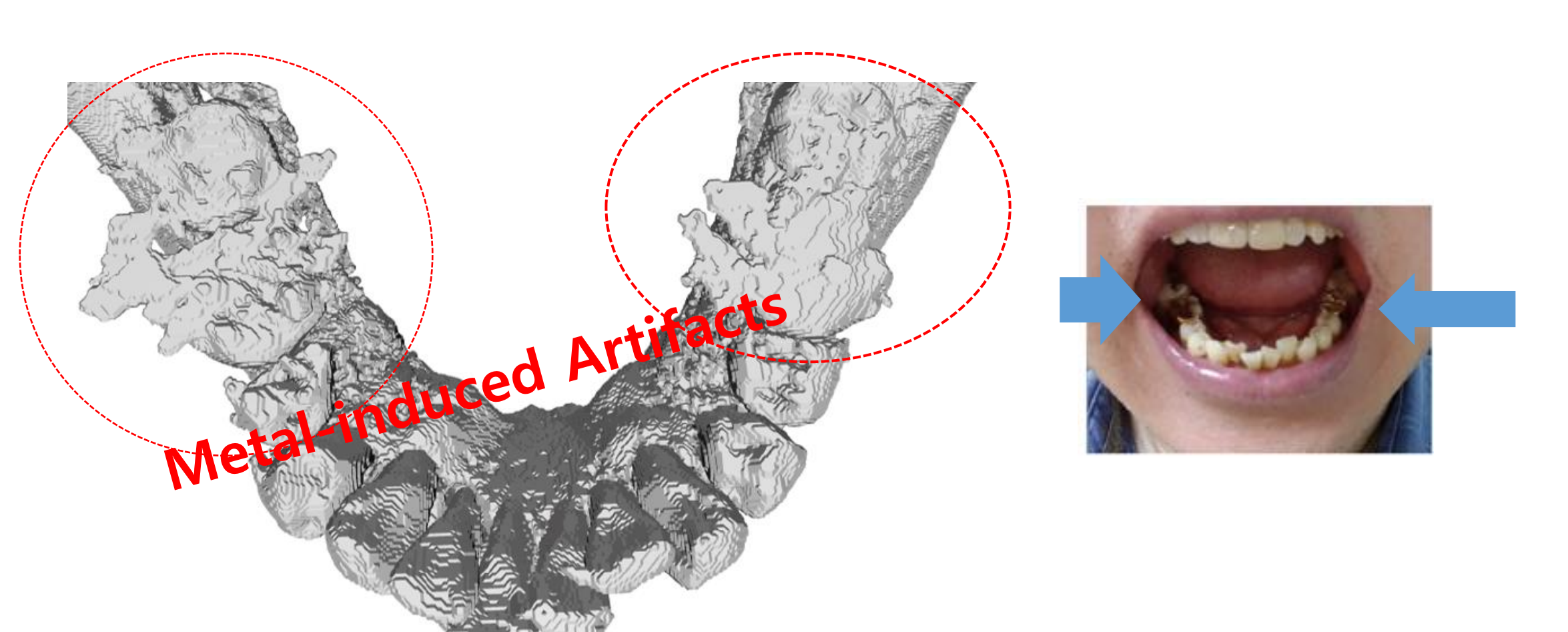
Why is the inverse problem of dental CBCT ill-posed & Nonlinear?

The actual CT model is polychromatic (NOT monochromatic):



Metal-induced Artifacts

- The accuracy of the linear forward model is compromised due to the idealized monochromatic assumption $(\eta(E) = \delta(E E_0))$.
- The presence of metal implants in CT scans leads to **severe discrepancies in the monochromatic assumption** of the X-ray data, resulting in metal artifacts.

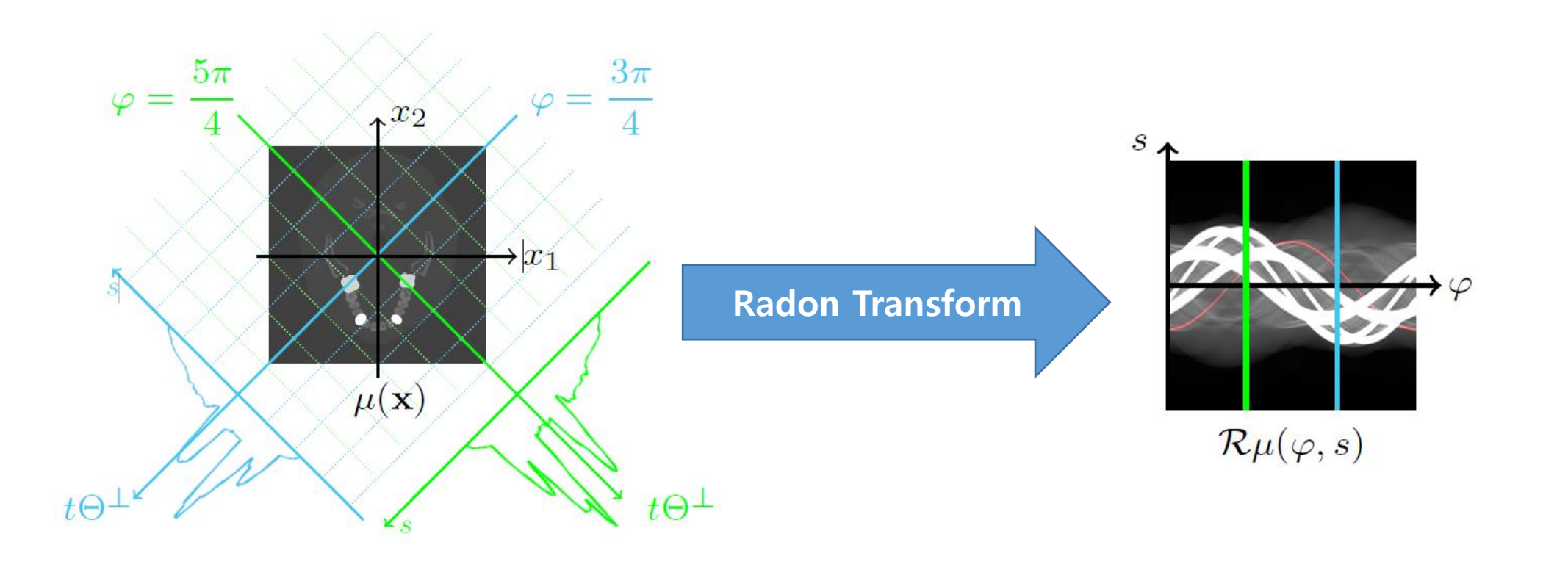


$$P(\varphi, u, v) = -ln \int \eta(E) \exp(-\mathcal{C}\mu_E(\varphi, u, v)) dE$$

To simplify our explanation, we will limit our discussion to the **2D parallel-** beam model with an idealized monochromatic assumption.

Radon Model

$$P(\varphi, s) = \mathcal{R}\mu(\varphi, s) = \int_{\mathbb{R}^2} \mu(x) \delta(x \cdot \Theta_{\varphi} - s) dx$$



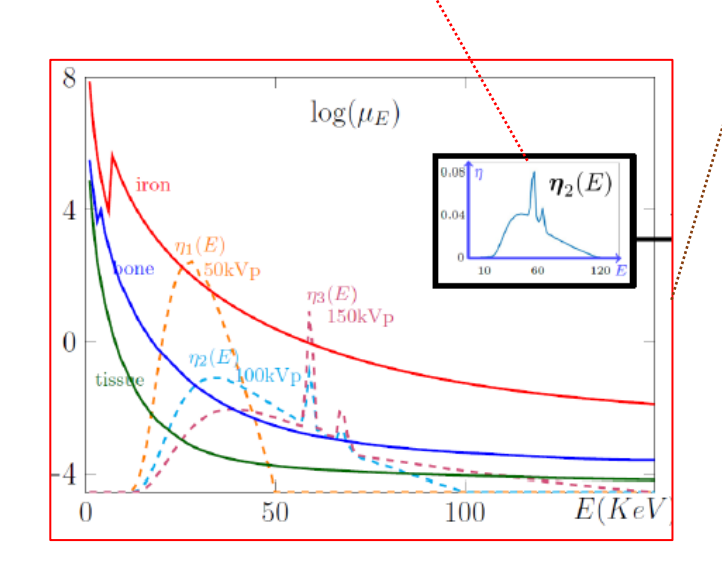
Although commercial CT scanners are **polychromatic**, research in the field of CT imaging largely relies on the simplifying assumption of a monochromatic Radon model.

Monochromatic Radon Model

$$P(\varphi, s) = \mathcal{R}\mu(\varphi, s) = \int_{\mathbb{R}^2} \mu(x) \delta(x \cdot \Theta_{\varphi} - s) dx$$

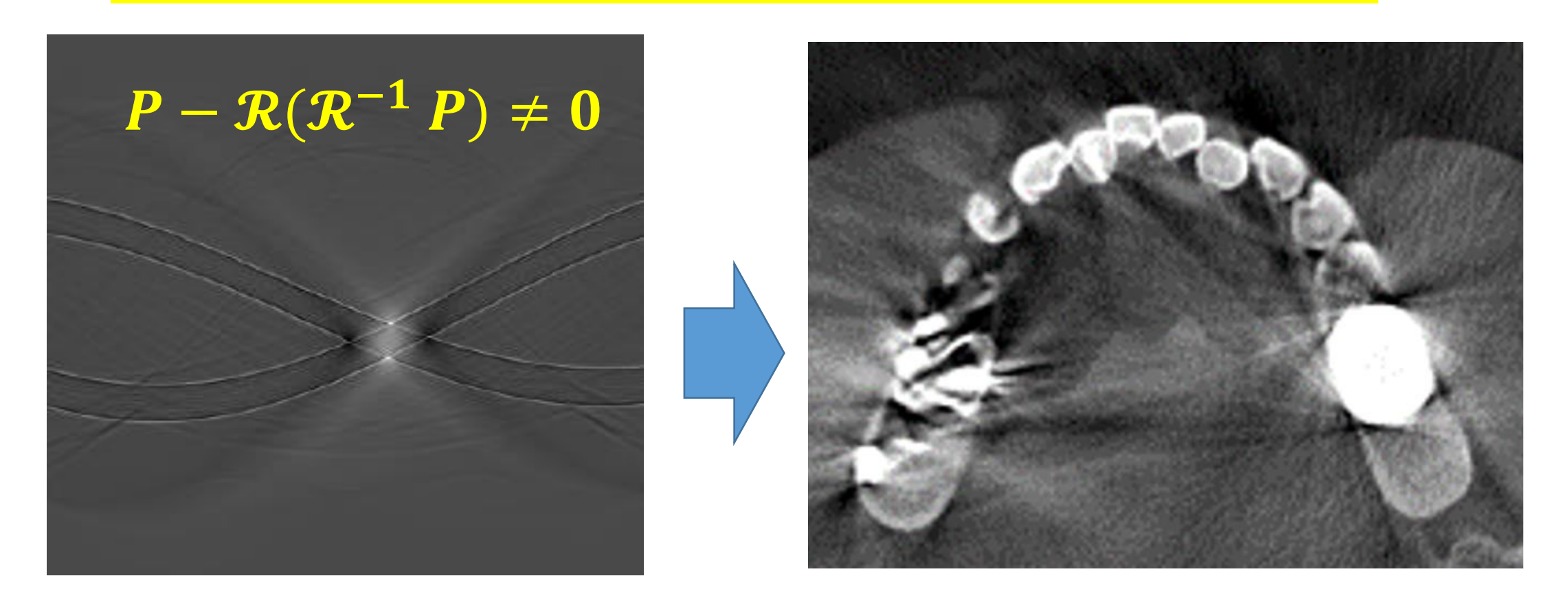
Polychromatic Actual Model

$$P(\varphi, s) = -\ln \int_{\gamma} \eta(E) \exp(-\Re \mu_E(\varphi, s)) dE$$



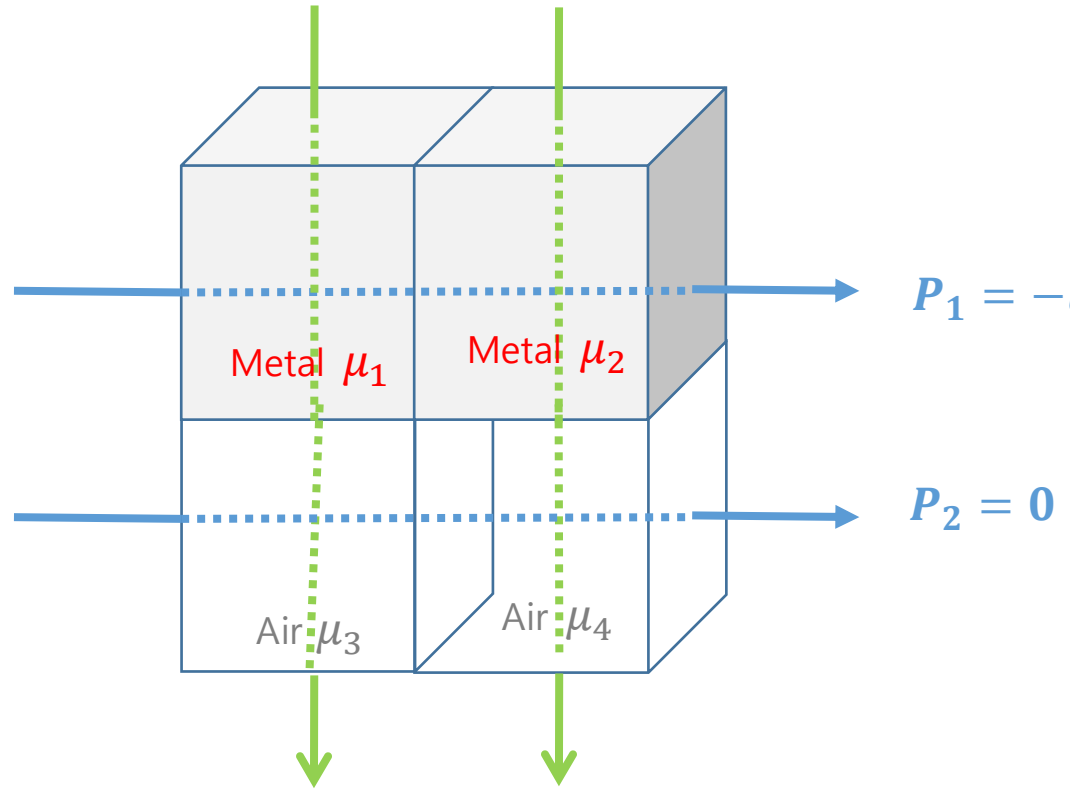
This model discrepancy can cause the acquired data **P** to fall outside the range of the Radon transform, indicating a discrepancy between the assumed model and the actual acquired data.

$$P = -\ln \int \eta(E) \exp(-\mathcal{R}\mu_E) dE \notin Range \ of \ \mathcal{R}$$



Toy model: bi-chromatic X-rays (64 and 80 KeV)

Metal object : $\mu_{64KeV} = 64$, $\mu_{80KeV} = 5$



$$P_3 = -log\left(\frac{1}{2}e^{-64} + \frac{1}{2}e^{-5}\right)$$

CT reconstruction problem based on Radon transform: Find $\mu \in R^4_+$ solving

$$\begin{pmatrix} 1 & 1 & 0 & 0 \\ 0 & 0 & 1 & 1 \\ 1 & 0 & 1 & 0 \\ 0 & 1 & 0 & 1 \end{pmatrix} \begin{pmatrix} \mu_1 \\ \mu_2 \\ \mu_3 \\ \mu_4 \end{pmatrix} = \begin{pmatrix} P_1 \\ P_2 = 0 \\ P_3 \\ P_3 \end{pmatrix}$$

$$P_1 = -log \left(\frac{1}{2} e^{-64 \times 2} + \frac{1}{2} e^{-5 \times 2} \right)$$

Answer: There exist no solution. Why? From 2nd low, $\mu_3=\mu_4=0$. From 3rd and 4th rows, $\mu_1=\mu_2$. From 1st row, μ_1 must satisfy

$$2\mu_1 = \mu_1 + \mu_2 = -log\left(rac{1}{2}e^{-64 imes 2} + rac{1}{2}e^{-5 imes 2}
ight)$$
 and $\mu_1 = -log\left(rac{1}{2}e^{-64} + rac{1}{2}e^{-5}
ight)$

This is not possible because

$$\left(\frac{1}{2}e^{-64} + \frac{1}{2}e^{-5}\right) \neq \sqrt{\frac{1}{2}e^{-64\times 2} + \frac{1}{2}e^{-5\times 2}}$$

$$P_1$$
 P_1
 $P_2 = 0$
 P_3
 $P_4 = P_3$

$$\begin{pmatrix} 1 & 1 & 0 & 0 \\ 0 & 0 & 1 & 1 \\ 1 & 0 & 1 & 0 \\ 0 & 1 & 0 & 1 \end{pmatrix} \begin{pmatrix} \mu_1 \\ \mu_2 \\ \mu_3 \\ \mu_4 \end{pmatrix} = \begin{pmatrix} P_1 = 12.5 \\ P_2 = 0 \\ P_3 = 7.5 \\ P_3 = 7.5 \end{pmatrix}$$

$$A \mu = P$$

What is
$$\mu = \underset{\mu}{argmin} ||A\mu - P||$$
 ?

 $\mu = (\mathbf{A}\mathbf{A}^*)^{-1}\mathbf{A}^*\mathbf{P}$

Reconstruction:
$$(AA^*)^{-1}A^*P^* = \begin{pmatrix} 10.2 \\ 2.9 \\ -3.4 \\ 4.0 \end{pmatrix} \neq \begin{pmatrix} a \\ a \\ 0 \\ 0 \end{pmatrix}$$

Steaking artifacts

Consider the problem
$$\begin{pmatrix} 1 & 1 & 0 & 0 \\ 0 & 0 & 1 & 1 \\ 1 & 0 & 1 & 0 \\ 0 & 1 & 0 & 1 \end{pmatrix} \begin{pmatrix} \mu_1 \\ \mu_2 \\ \mu_3 \\ \mu_4 \end{pmatrix} = \begin{pmatrix} P_1 \\ P_2 = 0 \\ P_3 \\ P_3 \end{pmatrix} \text{ with } P_1 = 3 \text{ and } P_3 = 2$$

$$\begin{pmatrix} 1 & 1 & 0 & 0 \\ 0 & 0 & 1 & 1 \\ 1 & 0 & 1 & 0 \\ 0 & 1 & 0 & 1 \end{pmatrix} \begin{pmatrix} \mu_1 \\ \mu_2 \\ \mu_3 \\ \mu_4 \end{pmatrix} = \begin{pmatrix} 3 \\ 0 \\ 2 \\ 2 \end{pmatrix} \qquad \qquad \begin{pmatrix} 1 & 1 & 0 & 0 \\ 0 & 0 & 1 & 1 \\ 1 & 0 & 1 & 0 \\ 0 & 1 & 0 & 1 \end{pmatrix} \begin{pmatrix} \mu_1 \\ \mu_2 \\ \mu_3 \\ \mu_4 \end{pmatrix} = \begin{pmatrix} 3 + \tilde{c} \\ -c \\ 2 - c \\ 2 + c \end{pmatrix} \qquad \qquad \mu = (\mathbf{A}\mathbf{A}^*)^{-1}\mathbf{A}^*\mathbf{P}$$

$$\begin{pmatrix} 1 & 1 & 0 & 0 \\ 0 & 0 & 1 & 1 \\ 1 & 0 & 1 & 0 \\ 0 & 1 & 0 & 1 \end{pmatrix} \begin{pmatrix} \mu_1 \\ \mu_2 \\ \mu_3 \\ \mu_4 \end{pmatrix} = \begin{pmatrix} 3 + c \\ -c \\ 2 - c \\ 2 + c \end{pmatrix}$$

streaking

Not in the range space of Radon transform

Project to the range space

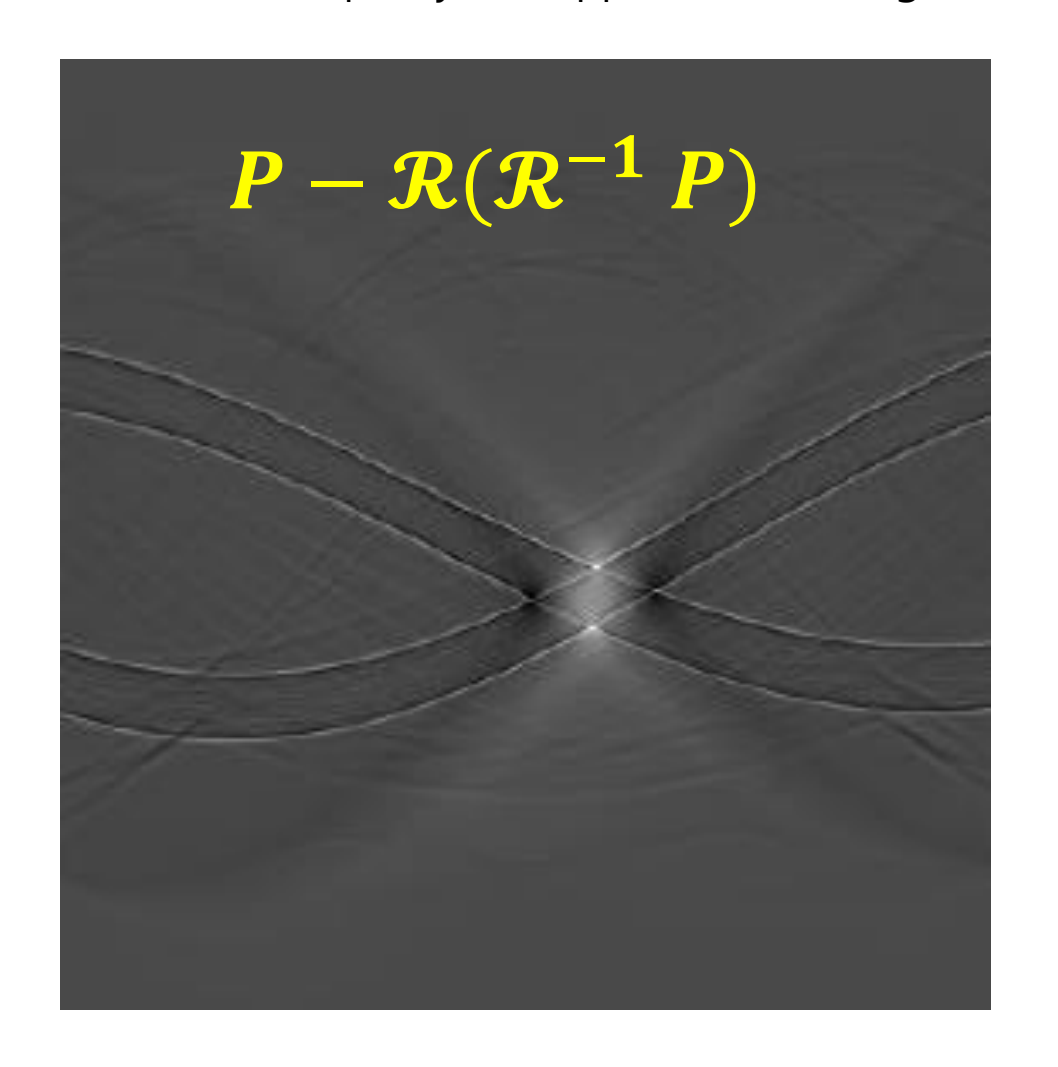
Question: How can we attain effective correction that significantly differs from the standard method?

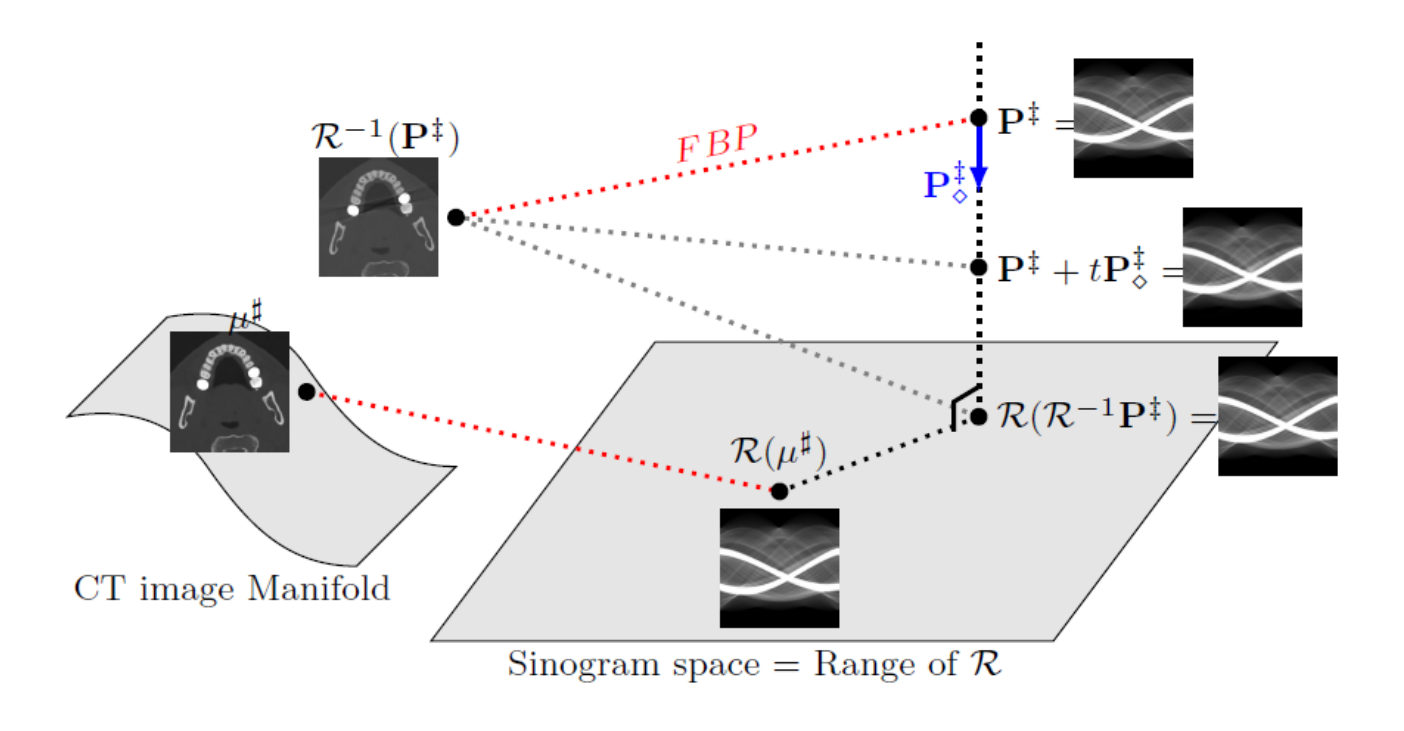
$$\begin{pmatrix} 1 & 1 & 0 & 0 \\ 0 & 0 & 1 & 1 \\ 1 & 0 & 1 & 0 \\ 0 & 1 & 0 & 1 \end{pmatrix} \begin{pmatrix} \mu_1 \\ \mu_2 \\ \mu_3 \\ \mu_4 \end{pmatrix} = \begin{pmatrix} 3 + 1 \\ 0 \\ 2 \\ 2 \end{pmatrix}$$

In metal artifact reduction in CT, correcting in sinogram space is challenging, therefore iterative approaches that incorporate both image space and sonogram space correction with regularization are commonly employed.

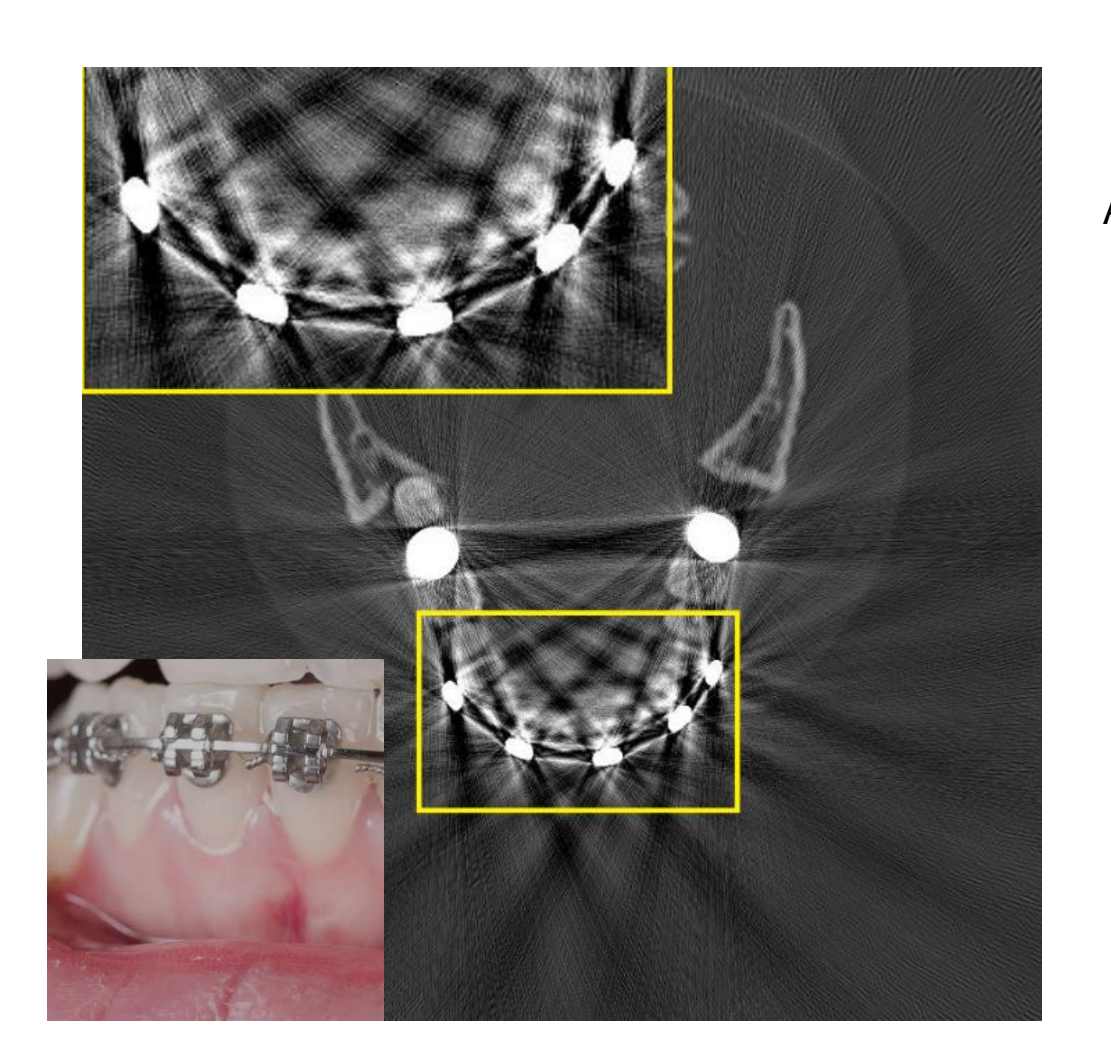
The mismatch $P - \mathcal{R}(\mathcal{R}^{-1} P) \neq 0$ produces metal artifacts.

- Based on the inherent nature of \mathcal{R}^{-1} , $\mathcal{R}(\mathcal{R}^{-1}P)$ is the closest sinogram in the range space of \mathcal{R} from P.
- According to Hilbert's projection theorem, the discrepancy $P \mathcal{R}(\mathcal{R}^{-1}P)$ is orthogonal to $Range\ of\ \mathcal{R}$.
- This discrepancy is mapped to streaking artifacts.





Handling metal-induced artifacts in dental CBCT is challenging due to complex factors related to metal-bone and metal-tooth interactions, FOV truncation, offset detector acquisition, scattering, non-linear partial volume effects, and others.



Artifact Expression due to the signogram inconsistency is:

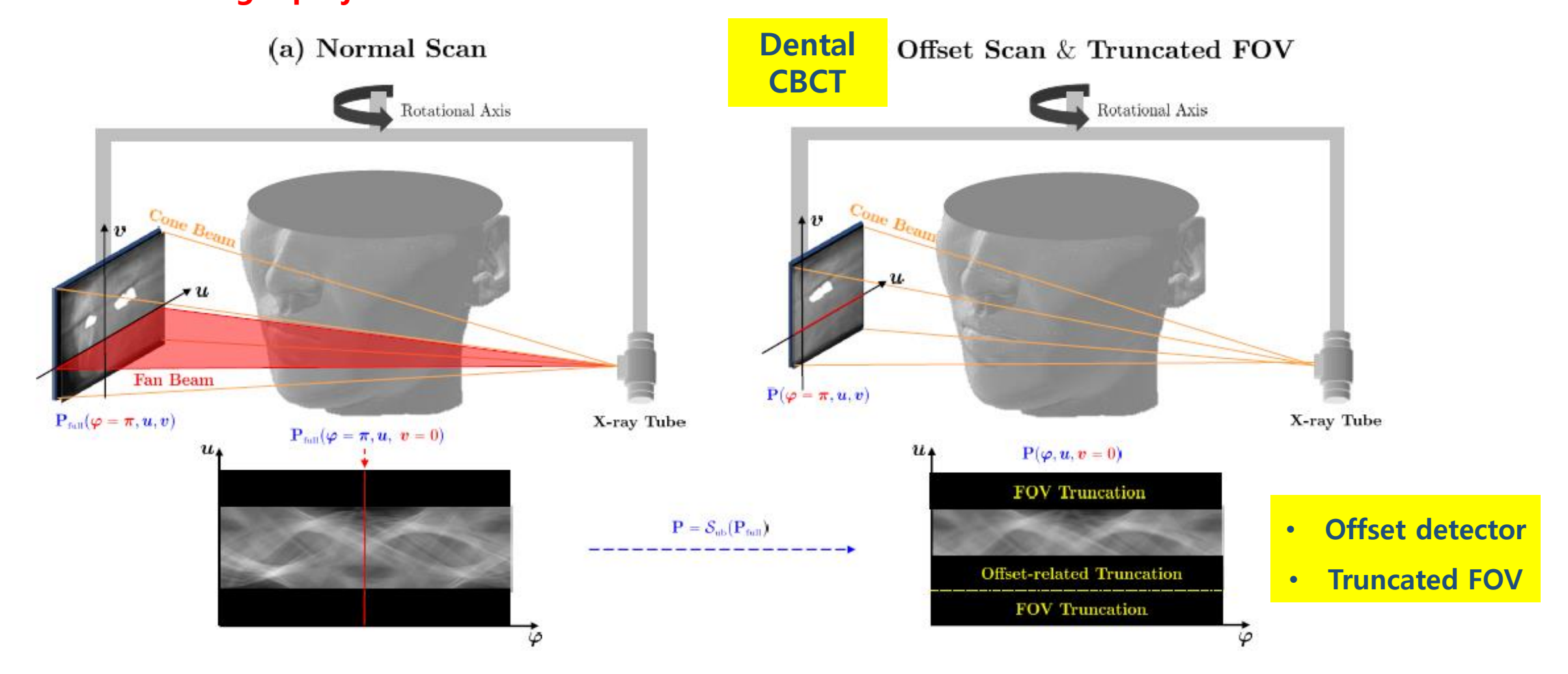
$$\mathbf{Y}(\mathbf{x}) = \iint \mathbf{\Gamma}_{\boldsymbol{\varphi},\mathbf{s}}(\mathbf{x}) \ \mathbf{P}^{\text{mismatch}}(\boldsymbol{\varphi},\mathbf{s}) \ d\mathbf{s} d\boldsymbol{\varphi}$$

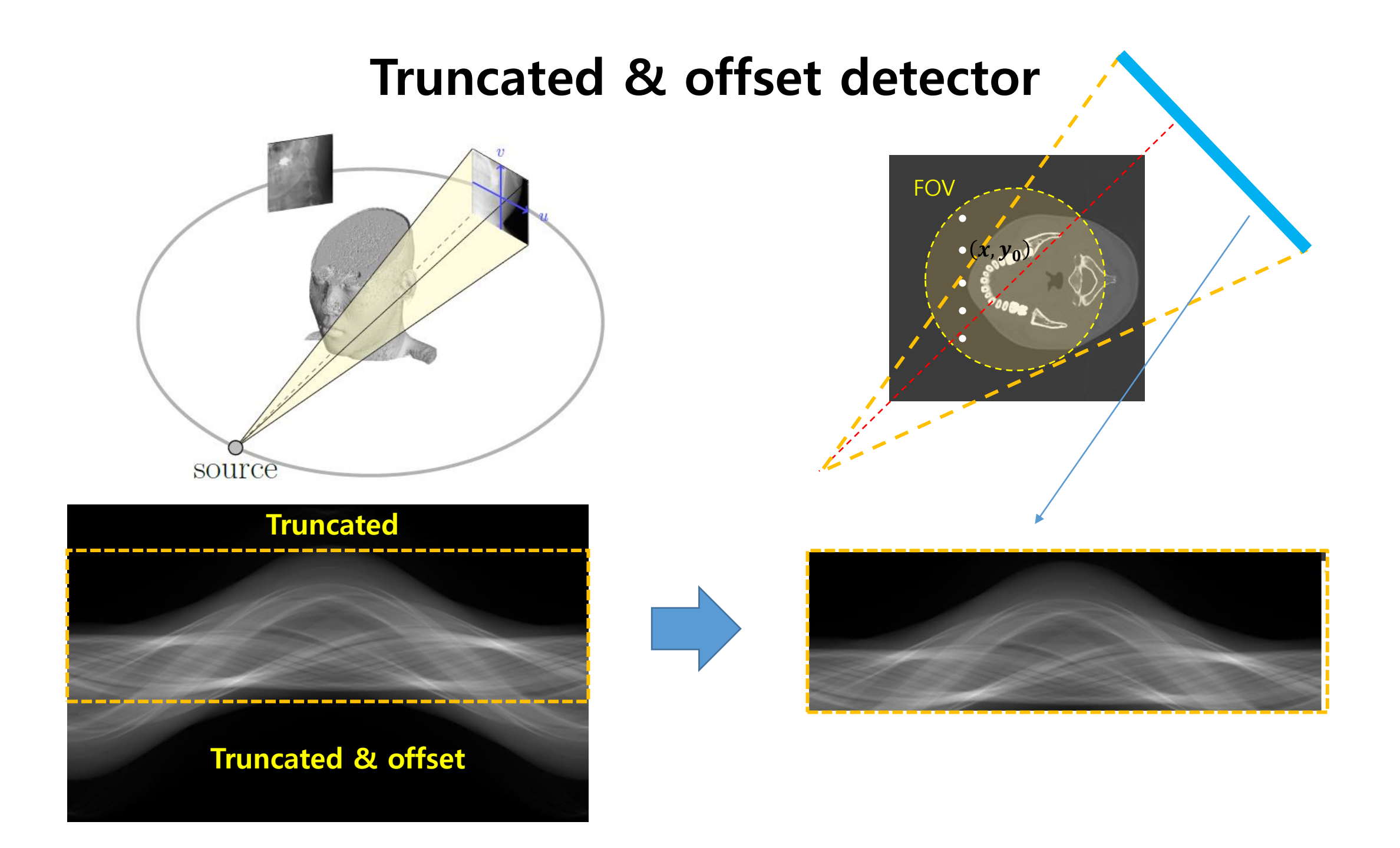
$$\Gamma_{\varphi,s} = \underset{\mu}{arg}\min || \delta_{\varphi,s} - R\mu ||$$

$$\mathcal{R}(\mathcal{R}^{-1}P^{ ext{mismatch}}) = \mathcal{R}(\mathcal{R}^{-1}P) - R\mu_*$$

Dental CBCT geometry

- The radiation beam of CBCT is cone-shaped, while that of conventional CT is fan-shaped.
- Typical dental CBCTs use offset detector to acquire only half of the extended FOV with a single projection.

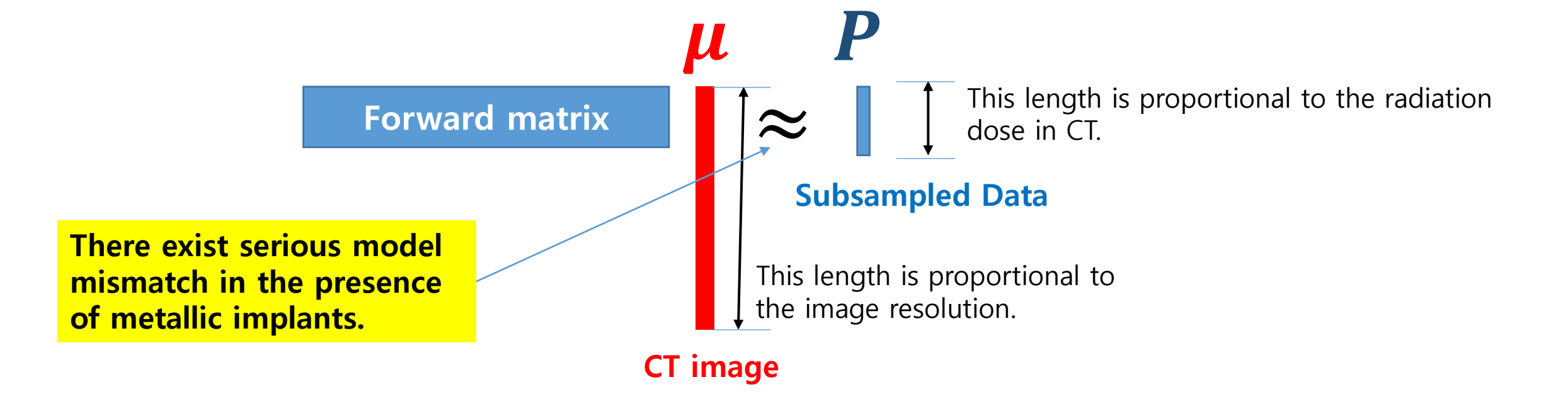




Why ill-posed?

As the demand to reduce the X-ray dose, the inverse problem of dental CBCT becomes increasingly ill-posed.

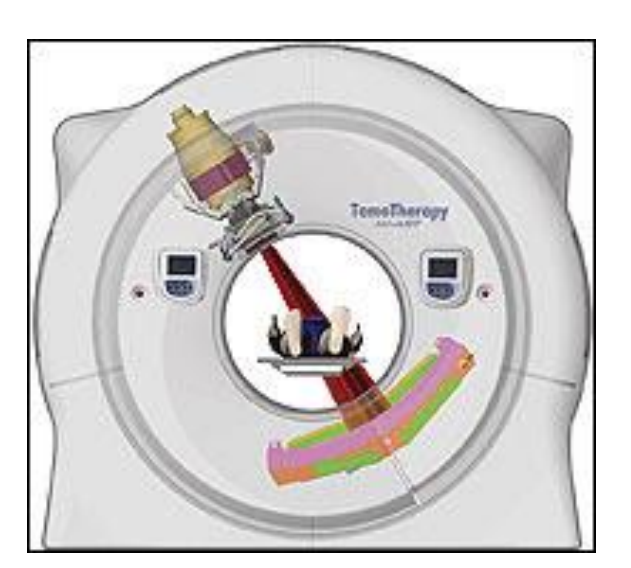
✓ We wish to make $\frac{\text{# of equations}}{\text{# of unknowns}}$ as small as possible to reduce radiation dose.



Motion artifacts are created by the long scan time of dental CBCT.

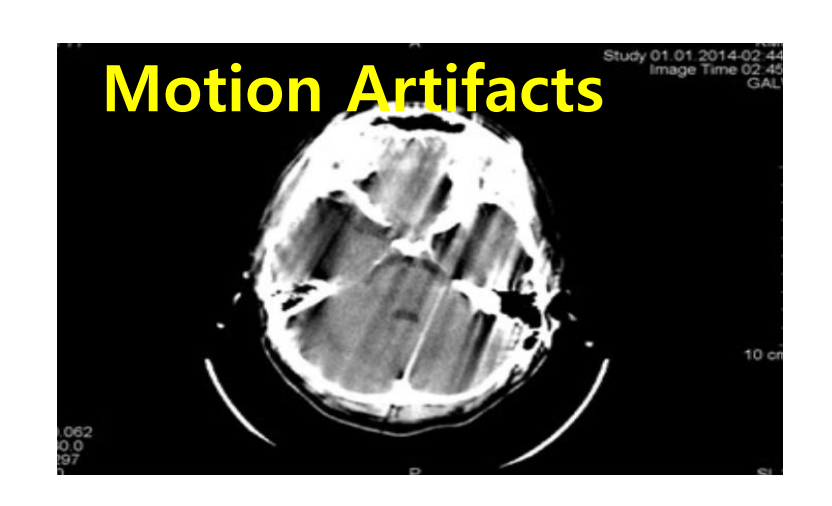
• Motion artifacts are caused by patient movement.

MDCT scan time: up to 0.25 sec

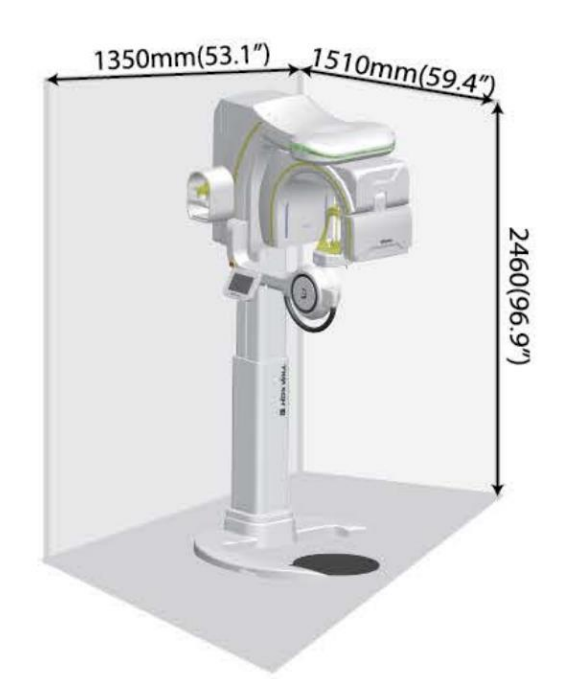


MDCT is not suitable for private dental clinics due to disadvantages such as high equipment cost and large space required for use.

Image Credit: MedWoW

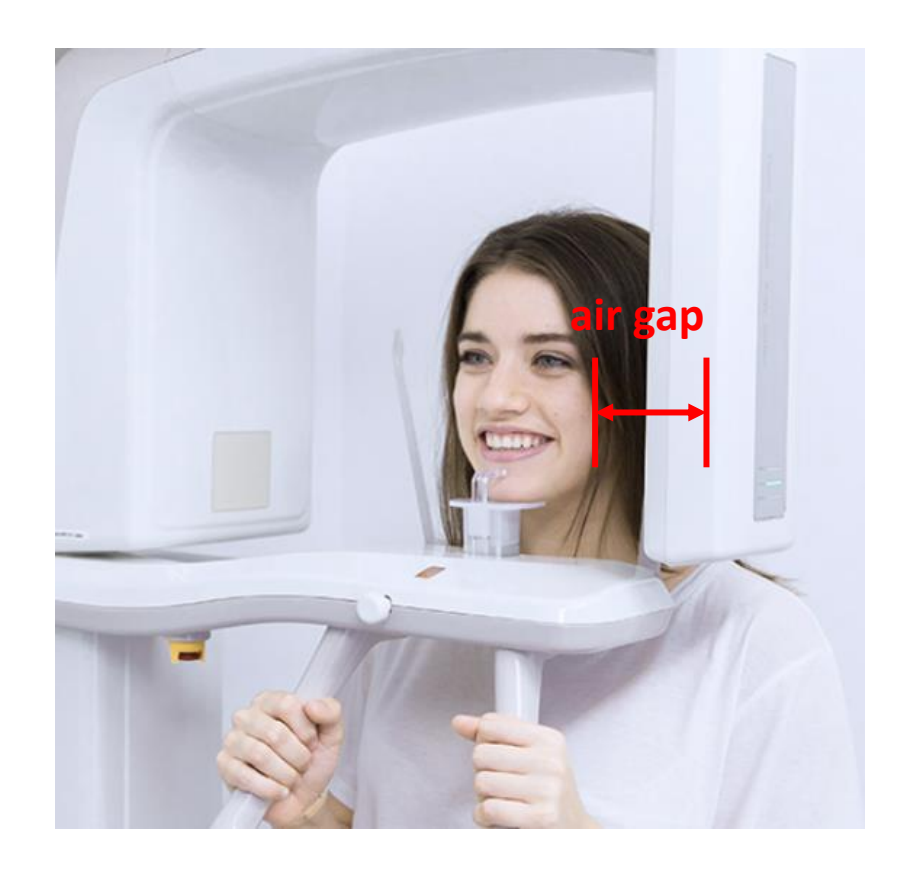


Dental CBCT Scan Time: 8.2 s (Normal) / 4.2 s (Fast)

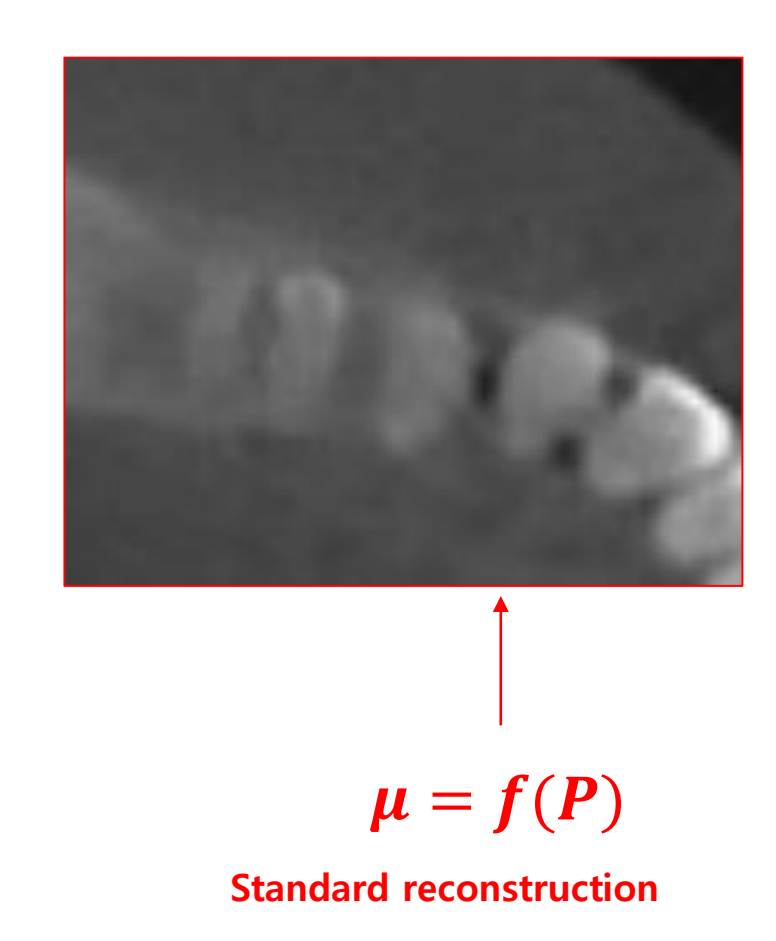


Scattering Artifacts due to the short air gap

In dental CBCT, the **object-to-detector distance** (ODD) is typically **as short as possible** in order to **increase the FOV**. In addition, shorter ODDs allow for the use of smaller detector areas (for cost saving).

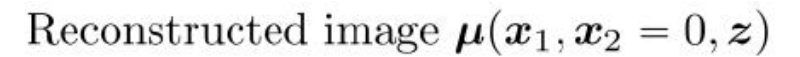


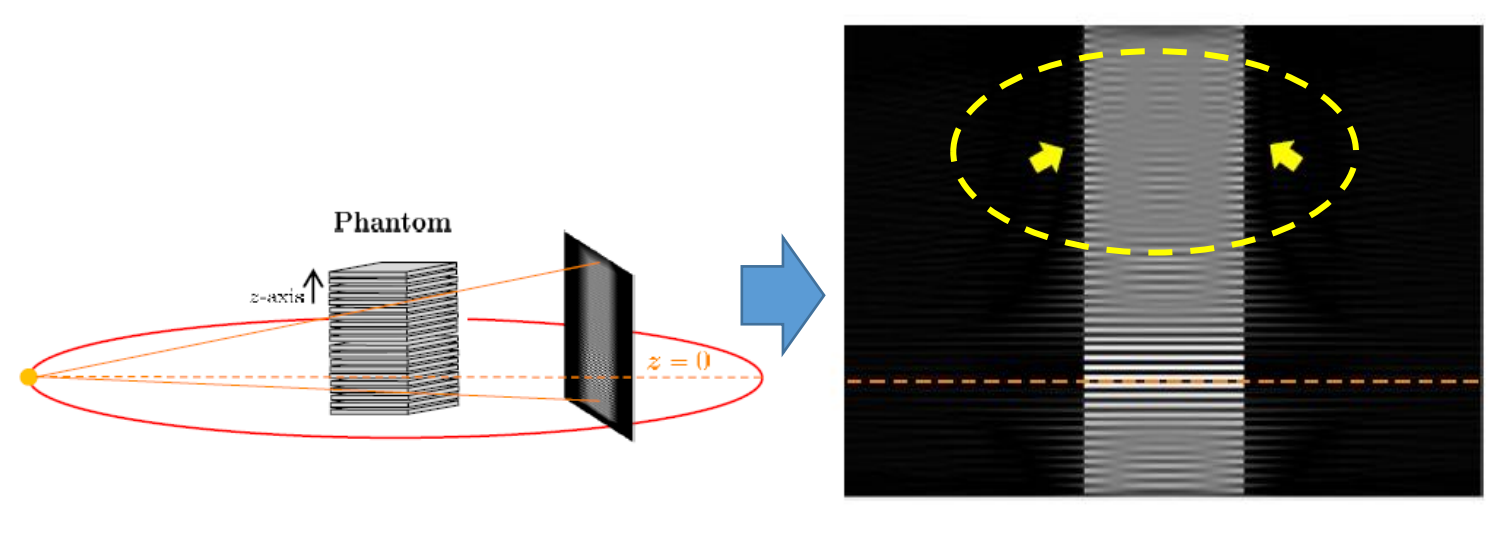
Due to the **short air gap (ODD)**, the most serious cause of artifacts is **scattering**. **As the air gap decreases**, the likelihood for **scattered x-ray radiation to reach the detector increases**.



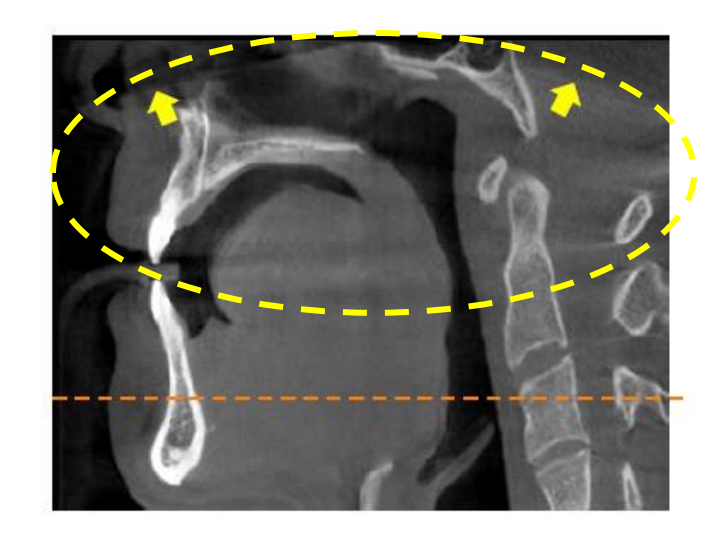
Cone beam artifacts: Violation of Tuy's data complete condition

Cone-beam artifacts are inherent to the circular scanning geometry that violates the data sufficiency condition formulated by Tuy. According to Tuy's condition, accurate reconstruction requires that every plain passing through any location in the region of interest (ROI) must intersect the source trajectory at least once.





Simulated CBCT



Clinical CBCT

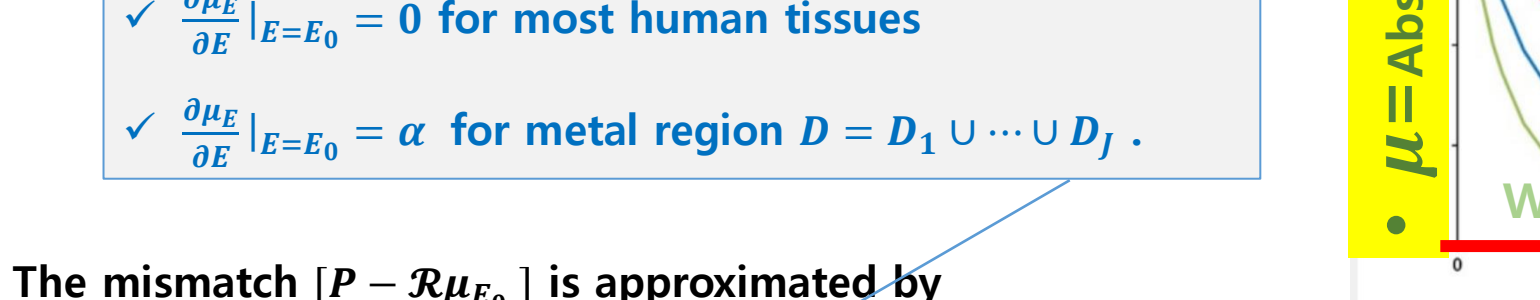
Mathematical characterization of metal artifacts

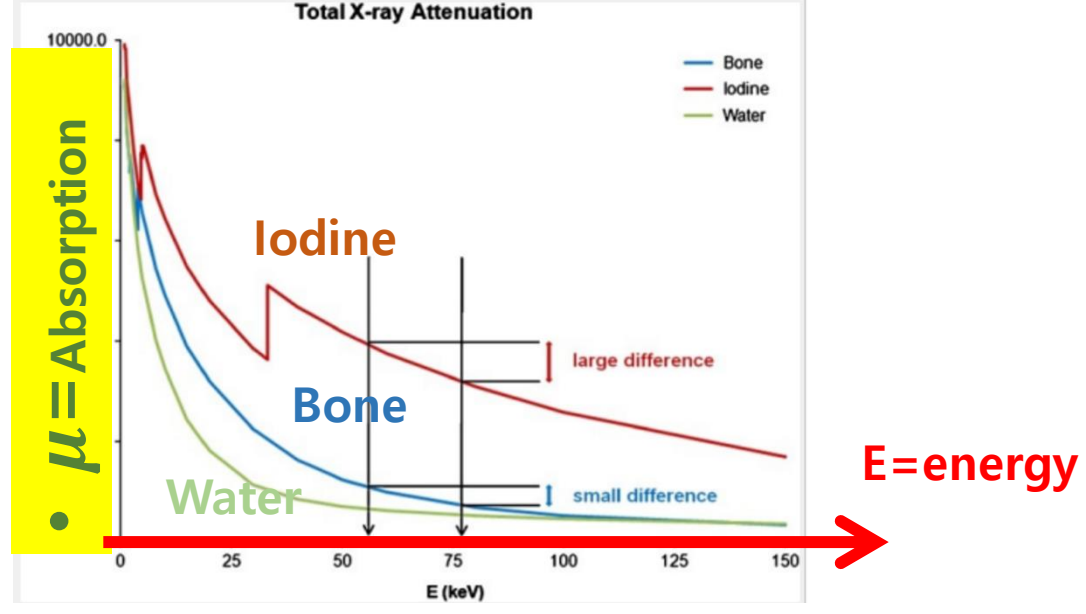
Mathematical characterization of metal artifacts

Linear Approximation w.r.t E

$$\mu_E(x) = \mu_{E_0}(x) + (E - E_0) \frac{\partial \mu_E}{\partial E} \Big|_{E = E_0} (x) + O(|E - E_0|^2)$$

$$\checkmark \frac{\partial \mu_E}{\partial E}|_{E=E_0} = \mathbf{0}$$
 for most human tissues





The mismatch $[P - \mathcal{R}\mu_{E_0}]$ is approximated by

$$\left[P - \mathcal{R}\mu_{E_0}\right] \approx -\ln\left(\int \eta(E) \exp\{-\alpha(E - E_0)\mathcal{R}\chi_D\} dE\right)$$

$$\approx -\ln\left(\int_{E_0 - h}^{E_0 + h} \frac{1}{2h} \exp\{-\alpha(E - E_0)\mathcal{R}\chi_D\} dE\right)$$

$$= -\ln\left(\frac{\sinh(\lambda \mathcal{R}\chi_D)}{\lambda \mathcal{R}\chi_D}\right)$$

- H. S. Park, J.K. Choi, J.K. Seo, Characterization of Metal Artifacts in X-ray Computed Tomography, CPAM (2017)
- H. S. Park, D.S. Hwang, J.K. Seo, Metal Artifacts Reduction for Polychromatic X-ray based on the Analytical Artifact Correction, IEEE TMI (2016)

Mathematical Form of Beam-hardening Artifact

Metal-induced artifacts induced by metals occupying the region $D = D_1 \cup D_2 \cup \cdots \cup D_J$ can be expressed as the following mathematical formula:

$$\phi_{D,\lambda}(x) = -\frac{1}{4\pi} \mathcal{R}^* I^{-1} \left[\ln \left(\frac{\sinh \left(\sum_{J=1}^J \lambda_J \mathcal{R} \chi_{D_J} \right)}{\sum_{J=1}^J \lambda_J \mathcal{R} \chi_{D_J}} \right) \right] (x)$$

$$\mathcal{R}^{-1} [P^{\ddagger}] \qquad \mathcal{R} \mu_{E_0}$$

- H. S. Park, J.K. Choi, J.K. Seo, Characterization of Metal Artifacts in X-ray Computed Tomography, CPAM (2017)
- H. S. Park, D.S. Hwang, J.K. Seo, Metal Artifacts Reduction for Polychromatic X-ray based on the Analytical Artifact Correction, IEEE TMI (2016)

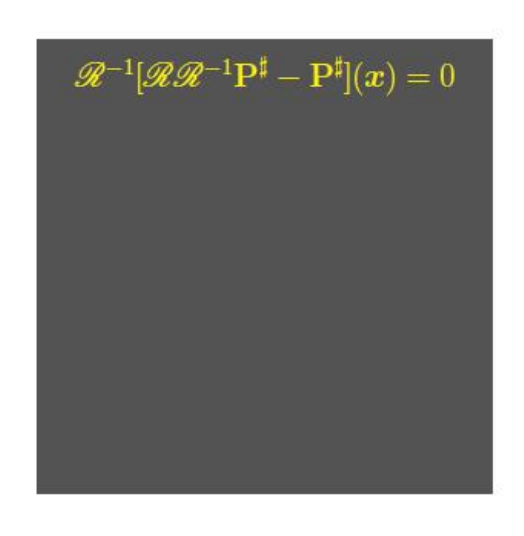
Visual explanation of metal-induced streaking artifacts using microlocal analysis

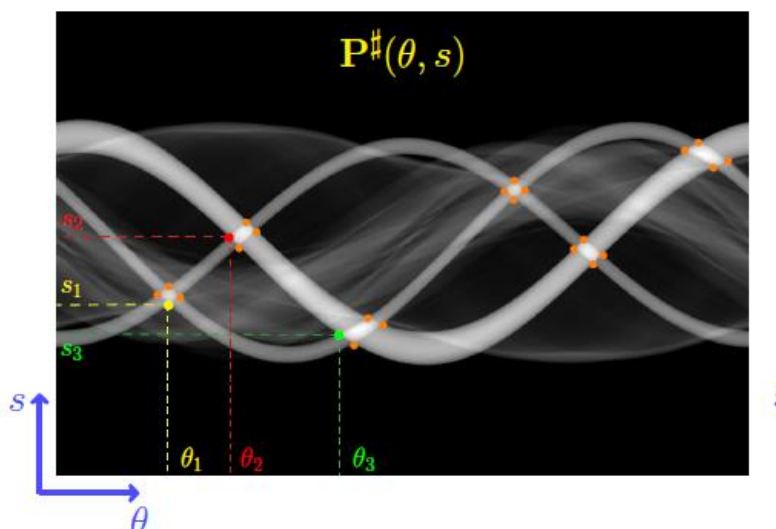
The metal streaking artifacts are produced only when the wavefront set of $\mathcal{R}\chi_D$ does not contain the wavefront set of $(\mathcal{R}\chi_D)^2$.

Hyoung Suk Park, Jae Kyu Choi, JinKeun Seo, Characterization of Metal Artifacts in X-ray Computed Tomography, CPAM (2017)

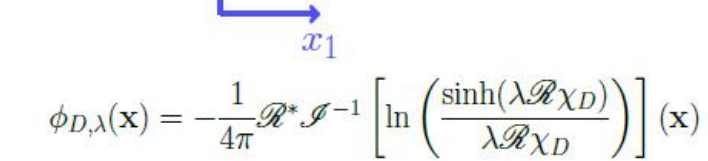


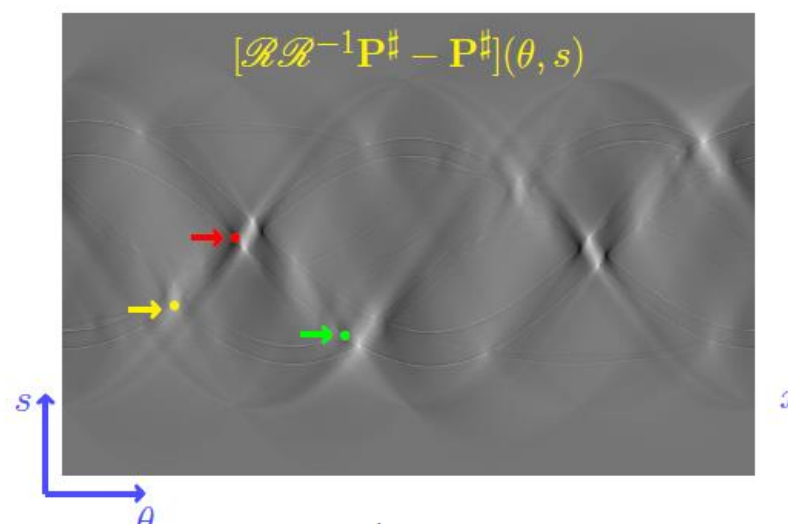
$$D = D_1 \cup D_2 \cup D_3$$



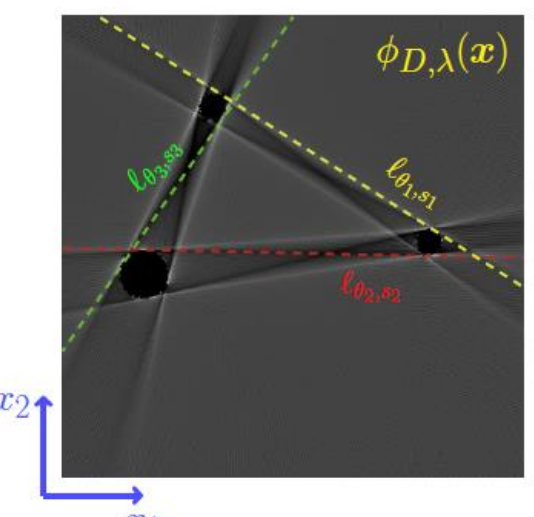


$$\dim(\operatorname{Span}[\Sigma_{(\theta_i,s_i)}(\mathscr{R}\chi_D)])=2$$

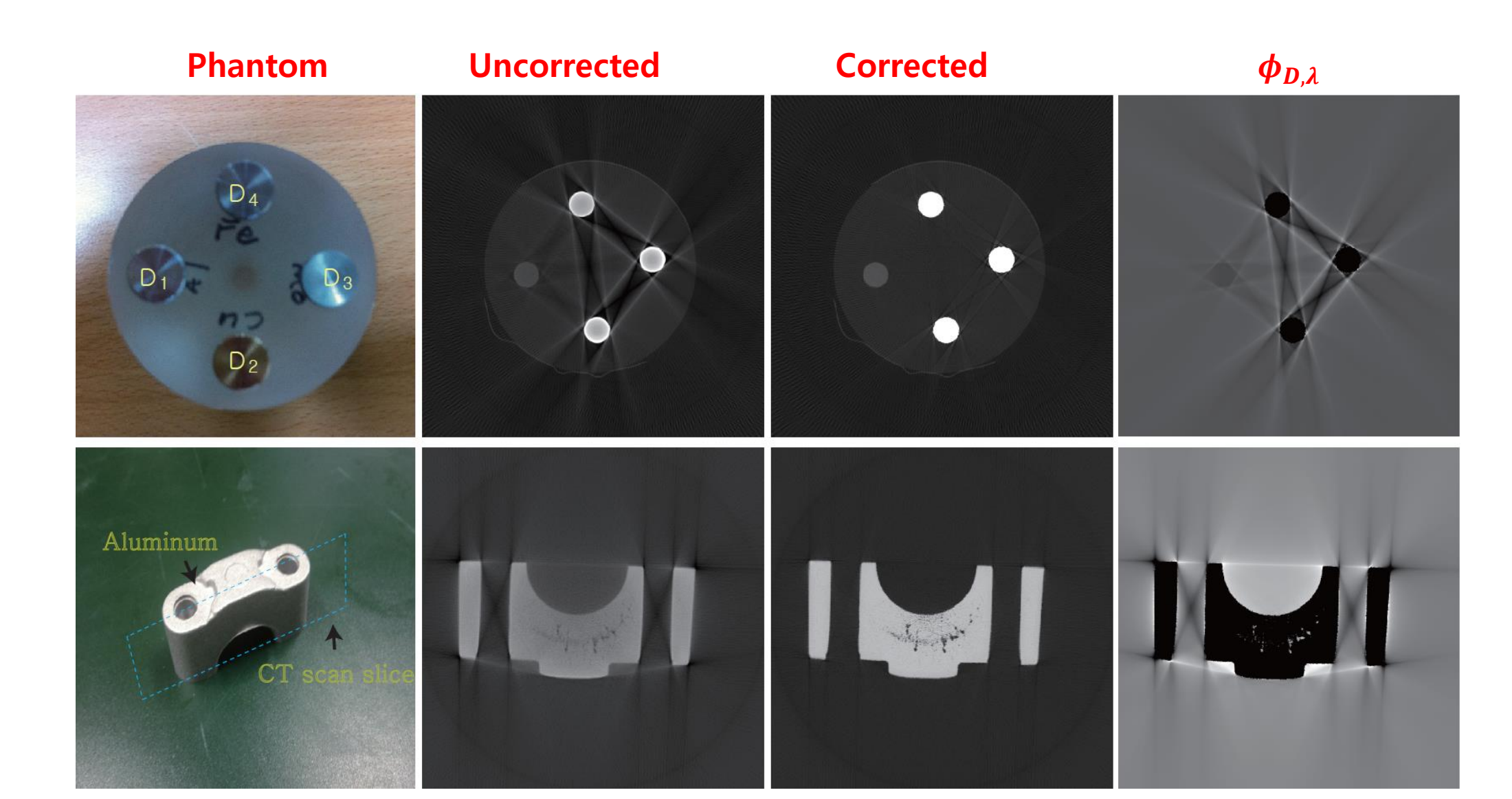




 \mathcal{I}^{-1} is the Riesz potential of degree -1.

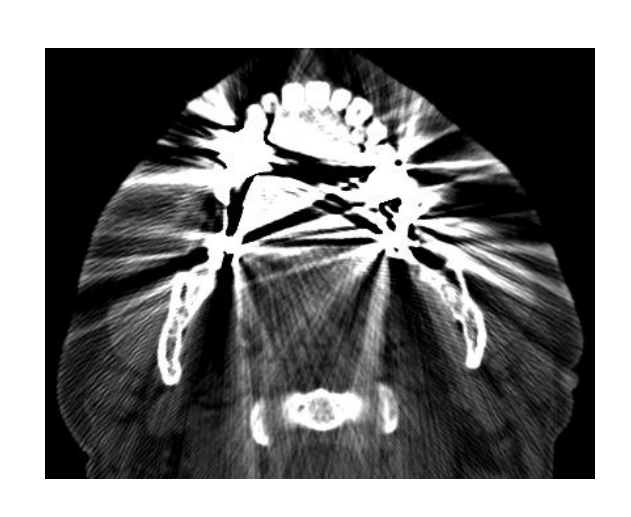


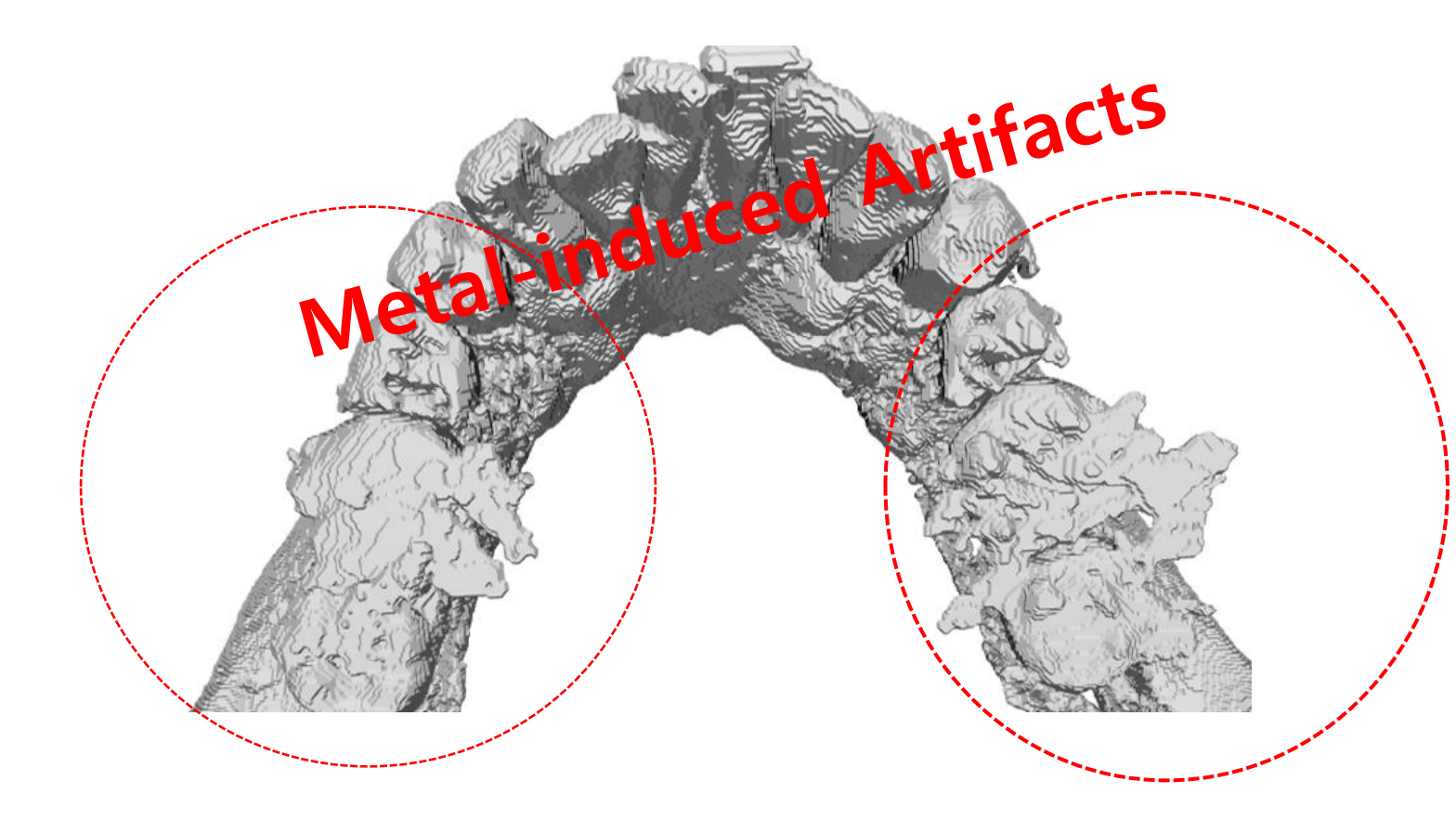
While the metal artifact corrector $\phi_{D,\lambda}$ has proven successful for MAR in industrial CBCT, it is less successful in dental CBCT due to additional factors such as metal-teeth interactions and FOV truncation.



Why is MAR(metal artifact reduction) difficult in clinical CBCT?

The artifact structure is not only non-linearly influenced by the local metal geometry, but is also entangled by complex factors related to metal-bone and metal-tooth interactions, FOV truncation, offset detector acquisition, scattering, non-linear partial volume effects, and others.





Regularization Methods

The standard regularization approach may not be effective in mitigating metal artifacts when metal implants occupy a significant portion of the imaged area.

$$\mu = \underset{\mu}{\operatorname{argmin}} ||P - R\mu||_{\ell^{2}}^{2} + Reg(\mu)$$

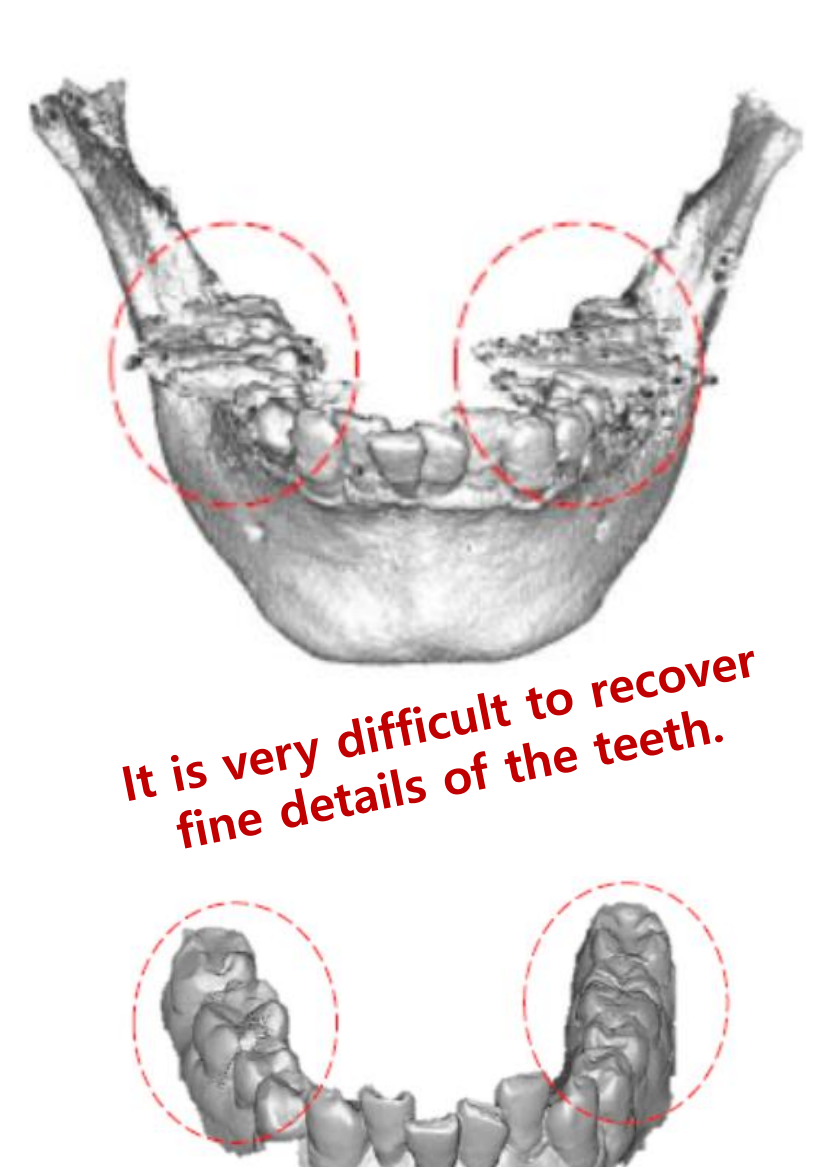
Regularization is an effective method for reducing noise in images. **NOT for this case.**

1. Conventional CS-based Regularization Methods

regularization

$$\mu_* = \underset{\mu}{\operatorname{argmin}} ||P - C\mu||_{\ell^2}^2 + \lambda \Gamma(\mu)$$

- The regularization $\Gamma(\mu)$ is expected to play a role in suppressing artifacts in the reconstructed image.
- $\Gamma(\mu)$ can be CS(compressed sensing) strategy, promoting sparsity in a given basis.
- CS-based regularizations cannot selectively preserve small details about teeth, due to the uniform penalization by $\lambda \Gamma(\mu)$.
- CS approaches tend to impair the morphological information of the region around the metallic object in the reconstructed image.



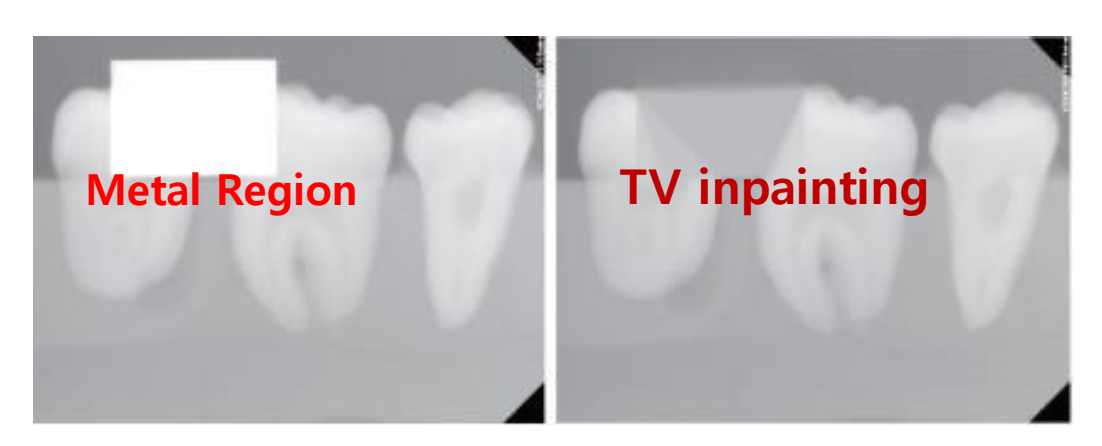
2. Inpainting-based sinogram correction

- Let **D** is metal region in the image space.
- The goal is to reconstitute the metal trace ($T = C\chi_D$) in the sonogram space.
- A sinogram correction P_{cor} can be obtained by minimizing the following objective function:

$$\mathcal{Loss}(\mathbf{P_{cor}}) := ||(P_{cor} - P) \odot \chi_{T^c}||_{\ell^2}^2 + \lambda ||\nabla P_{cor}||_{\ell^1}$$

- • is Hadamard's product
- χ_{T^c} is is the binary mask of the sinogram area excluding the metal trace

These sinogram correction methods have been somewhat successful, but these methods can create new artifacts that were not there before.







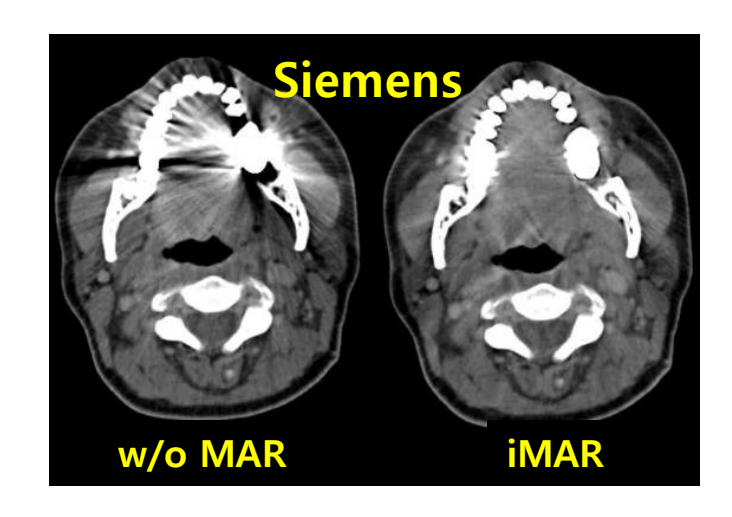
3-1. Iterative Reconstruction for MAR (metal artifact reduction)

• Artifact reduction:
$$\mu^{(k+\frac{1}{2})} = \mu^{(k)} - \gamma \nabla \Gamma(\mu^{(k)})$$
 plays a key role to extract artifacts and noise.

• Data fidelity:
$$\mu^{(k+1)} = \underset{\mu}{\operatorname{argmin}} ||(P - \mathcal{C}\mu) \odot \chi_{T^c}||_{\ell^2}^2 + \frac{\lambda}{\gamma} ||\mu - \mu^{\left(k + \frac{1}{2}\right)}||$$

There are two questions:

- (i) Which regularization is most appropriate? Hand-craft regularization priors such as total variation seem to have limited performance in handling artifacts that have nonlinear structure depending on a variety of metal geometries.
- (ii) Is it appropriate to use the same regularization in each iteration? Since artifacts and noise characteristics are different for each iteration step, it would be desirable to use a different artifact corrector for each iteration step.



3-2. Iterative reconstruction with data-driven regularization

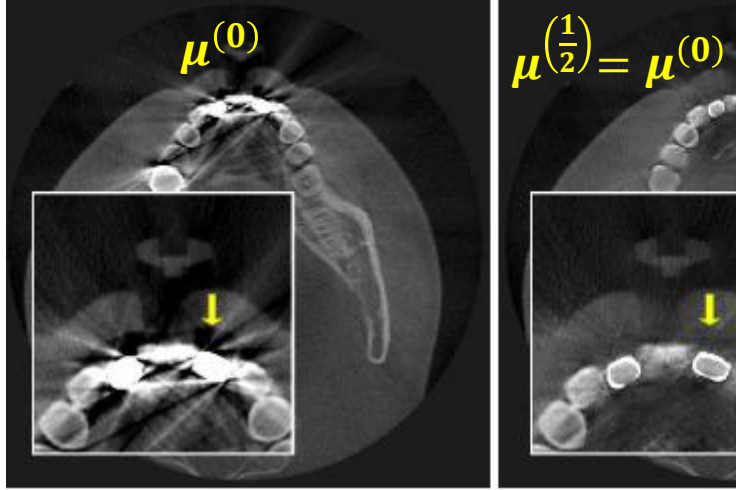
Artifact extractor $\gamma \nabla \Gamma(\mu^{(k)})$ is replaced by $f^{(k)}(\mu^{(k)})$. • $\mu^{\left(k+\frac{1}{2}\right)} = \mu^{(k)} \leftarrow \gamma \nabla \Gamma(\mu^{(k)})$

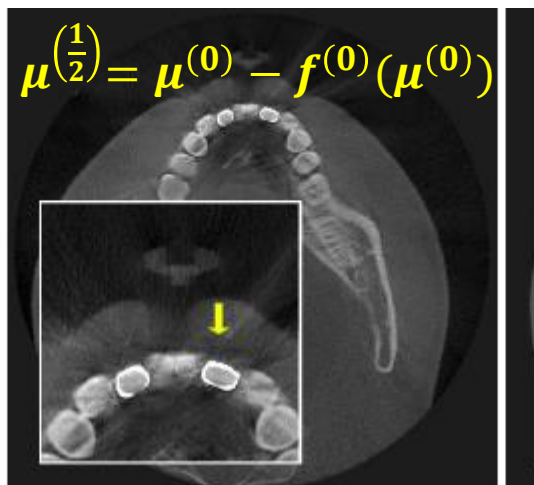
•
$$\mu^{(k+1)} = \underset{\mu}{\operatorname{argmin}} ||(P - C\mu) \odot \chi_{T^c}||_{\ell^2}^2 + \frac{\lambda}{\gamma} ||\mu - \mu^{(k+\frac{1}{2})}||$$

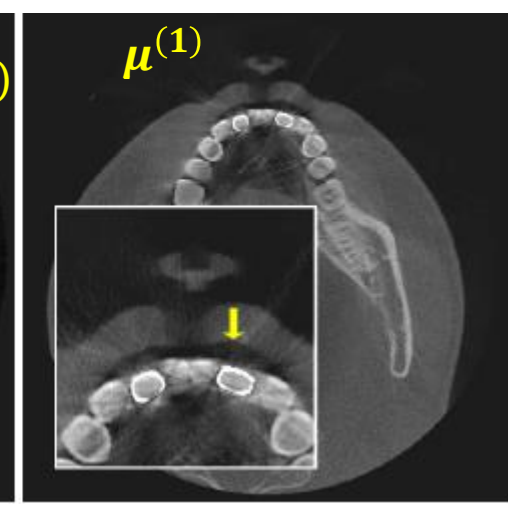
Learn $f^{(k)}: \mu^{(k)} \to \zeta^{(k)}$ using paired data $S^{(k)} = \{ (\mu_i^{(k)}, \zeta_i^{(k)}) : i = 1, \dots, L \}$ by

$$f^{(k)} = \underset{f \in NN}{\operatorname{argmin}} \frac{1}{L} \sum_{i=1}^{L} ||f(\mu_i^{(k)}) - \zeta_i^{(k)}||^2$$

How can we get the paired Training data?



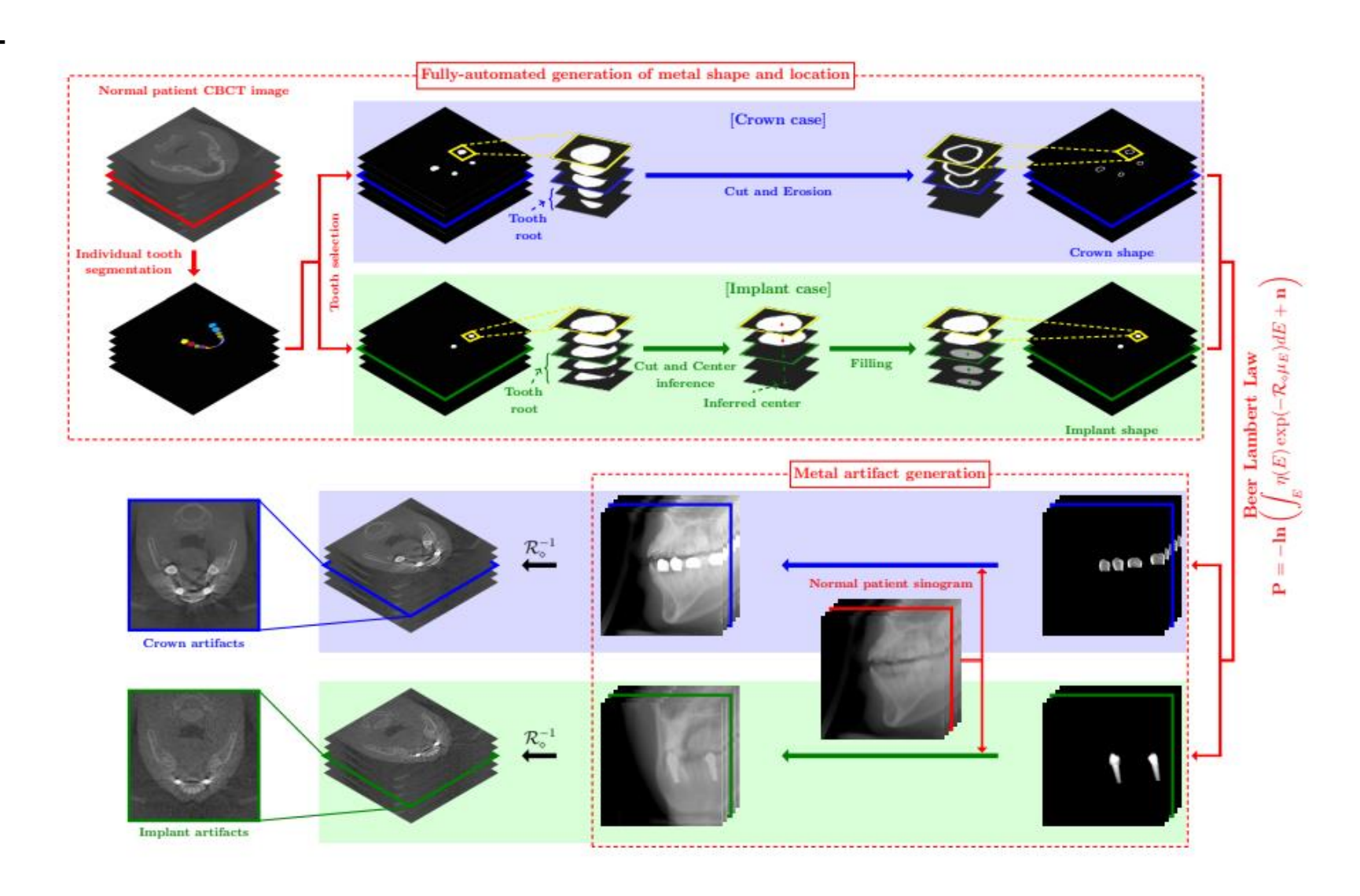




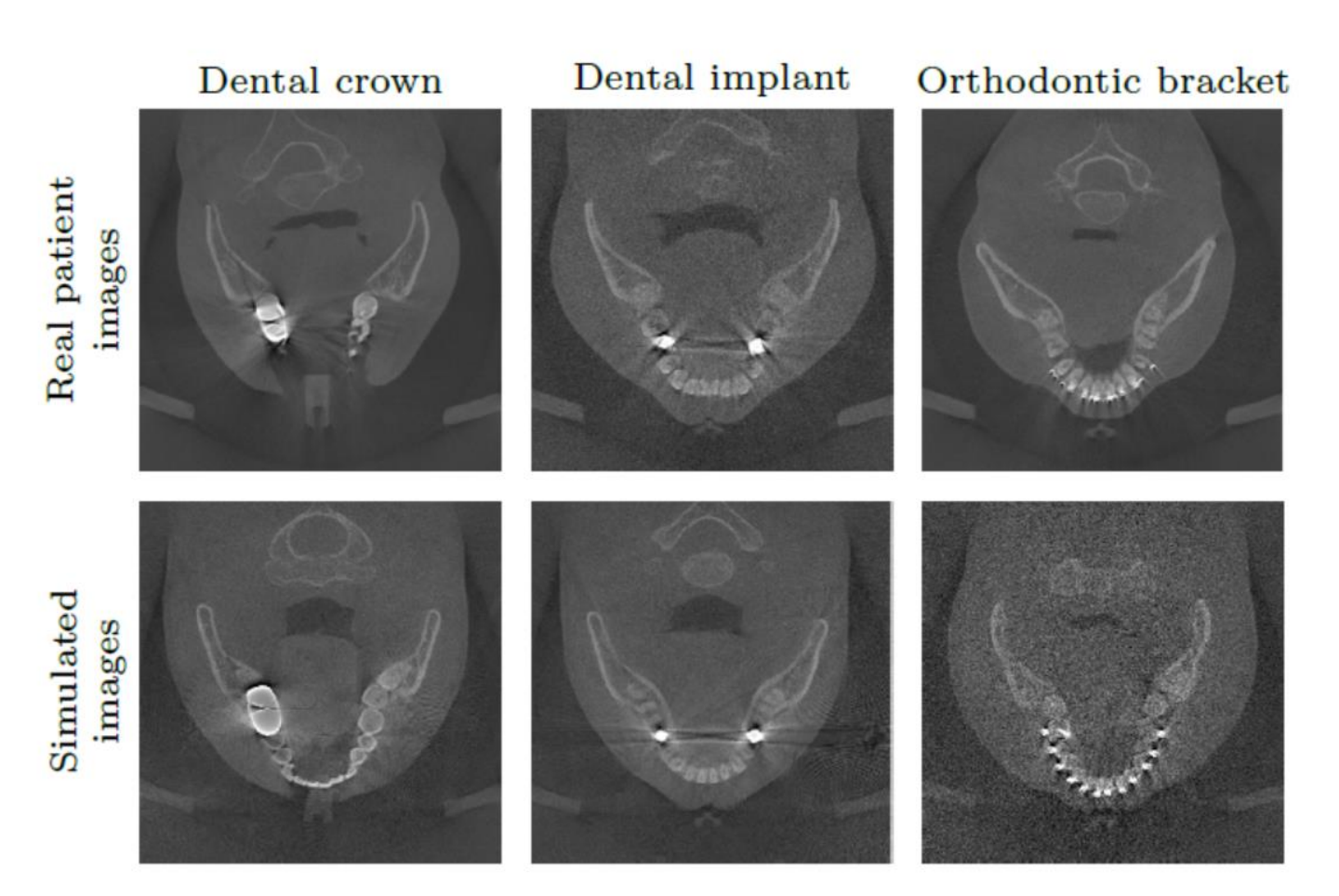
3-3. How to get paired training data $S^{(k)} = \{ (\mu_i^{(k)}, \zeta_i^{(k)}) : i = 1, \dots, L \}$

Use a combination of artifactfree real data and simulated artifacts

- 1. From artifact-free image, apply individual tooth segmentation (YOLO, U-Net)
- 2. Metal implant shape generation
- Metal artifact generation (using accurate Forward model)
- 4. GAN-based synthetic-to-realistic image refinement



Supervised DL methods appear to work very well. But, due to difficulty in generating realistic paired data, these methods have limited performance for clinical data.



- The simulated images look very realistic, but in reality they are different.
 - It is difficult to generate realistic paired data.

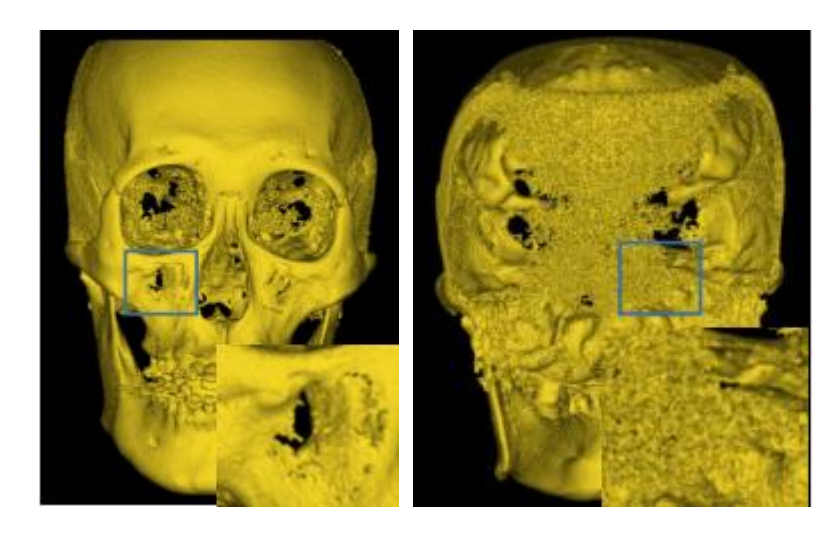
4-1. Unsupervised Learning Approach: Least S_{quare} $G_{enerative}$ $A_{dversarial}$ N_{etwork}

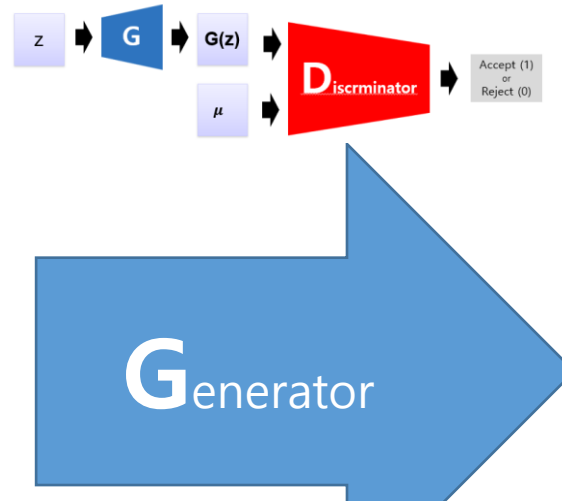
- Use GAN along with the fidelity difference between the original CBCT (its probability distribution p_{CBCT}) and MDCT-like images (p_{MDCT}) generated by the network. This approach is generally effective for denoising.
- But it can introduce additional artifacts because **the weak input fidelity between the two imaging modalities** can make it difficult to preserve the morphological structures from complex shadowing artifacts..

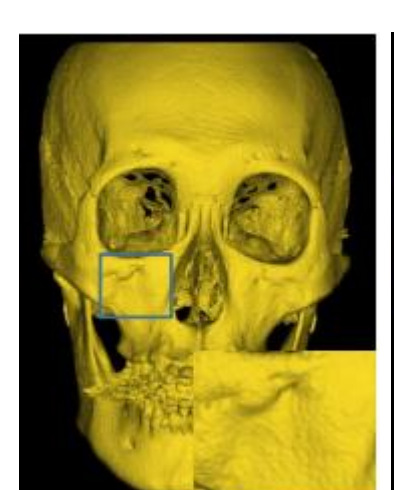
$$G = \underset{G}{\operatorname{argmin}} E_{z \sim p_{CBCT}} \left[\left(D \circ G(z) \right)^{2} \right] + \lambda E_{z \sim p_{CBCT}} \left[\left| \left[G(z) - z \right| \right] \right]$$

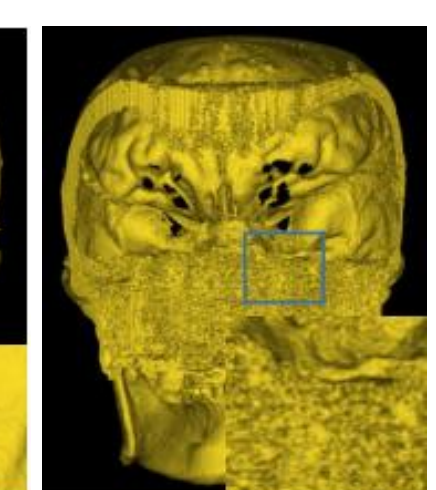
$$D = \underset{D}{\operatorname{argmin}} E_{\mu \sim p_{MDCT}} \left[\left(1 - D(\mu) \right)^{2} \right] + \lambda E_{z \sim p_{CBCT}} \left[\left(1 + D \circ G(z) \right)^{2} \right]$$

 $z \sim p_{\textit{CBCT}}$ (CBCT image)









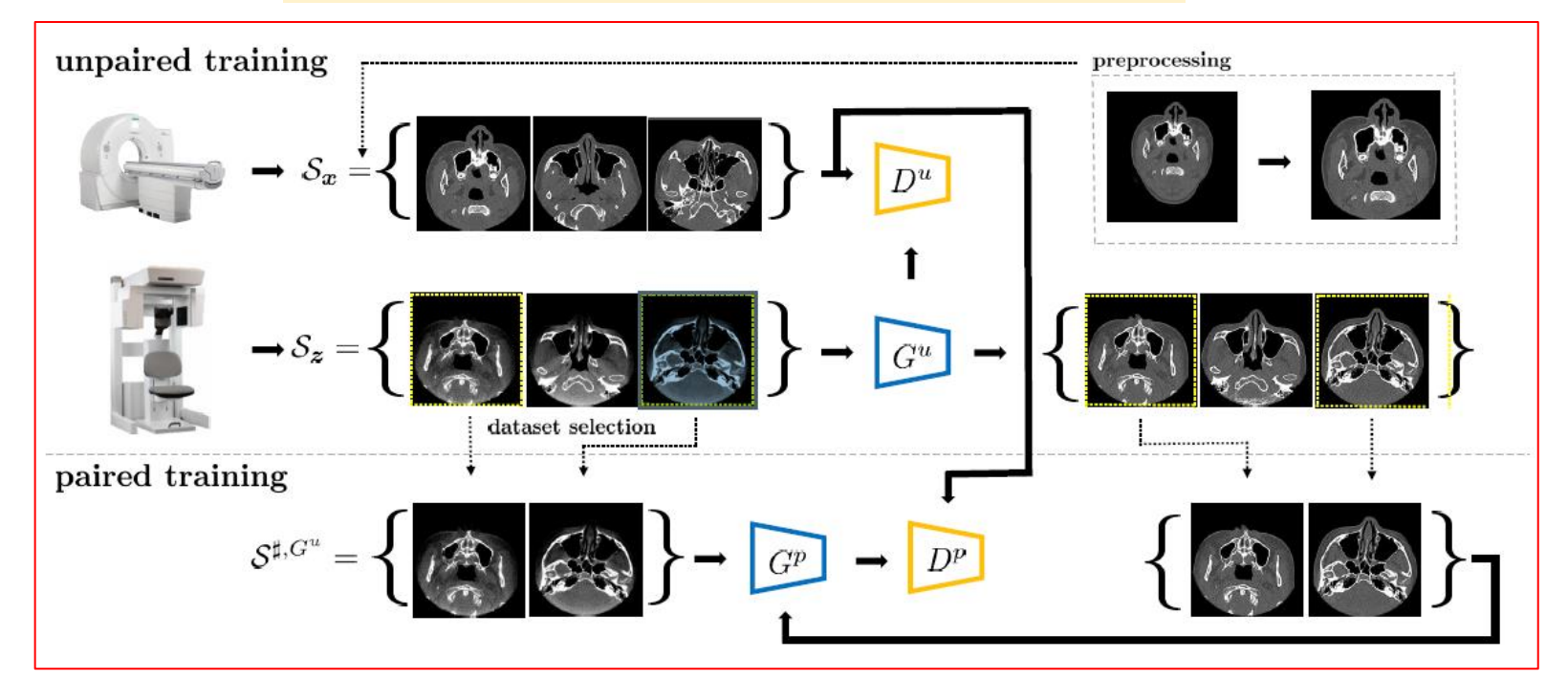
G(z) (MDCT-like image)

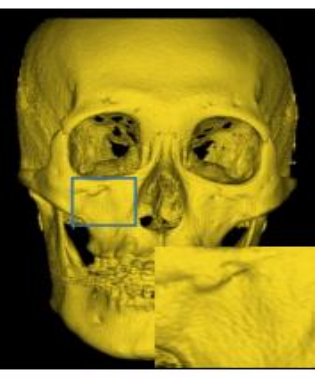
4-2. To address the problem of the weak input fidelity between the two imaging modalities, we adopt unpaired-paired learning.

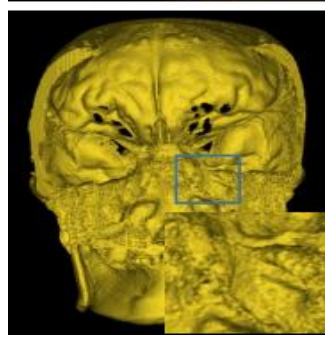
- Paired training data, excluding inappropriate data, were collected from the results obtained in the first stage.
- Subsequently, the fidelity-embedded GAN was retrained using the selected paired samples.

$$G = \underset{G}{\operatorname{argmin}} E_{z \sim p_{CBCT}} \left[\left(D \circ G(z) \right)^{2} \right] + \lambda E_{z \sim p_{CBCT}} \left[||G(z) - z|| \right]$$

$$D = \underset{D}{\operatorname{argmin}} E_{\mu \sim p_{MDCT}} \left[\left(1 - D(\mu) \right)^{2} \right] + \lambda E_{z \sim p_{CBCT}} \left[\left(1 + D \circ G(z) \right)^{2} \right]$$







- This method is very effective in removing scattering noise.
- However, this is not useful for MAR.

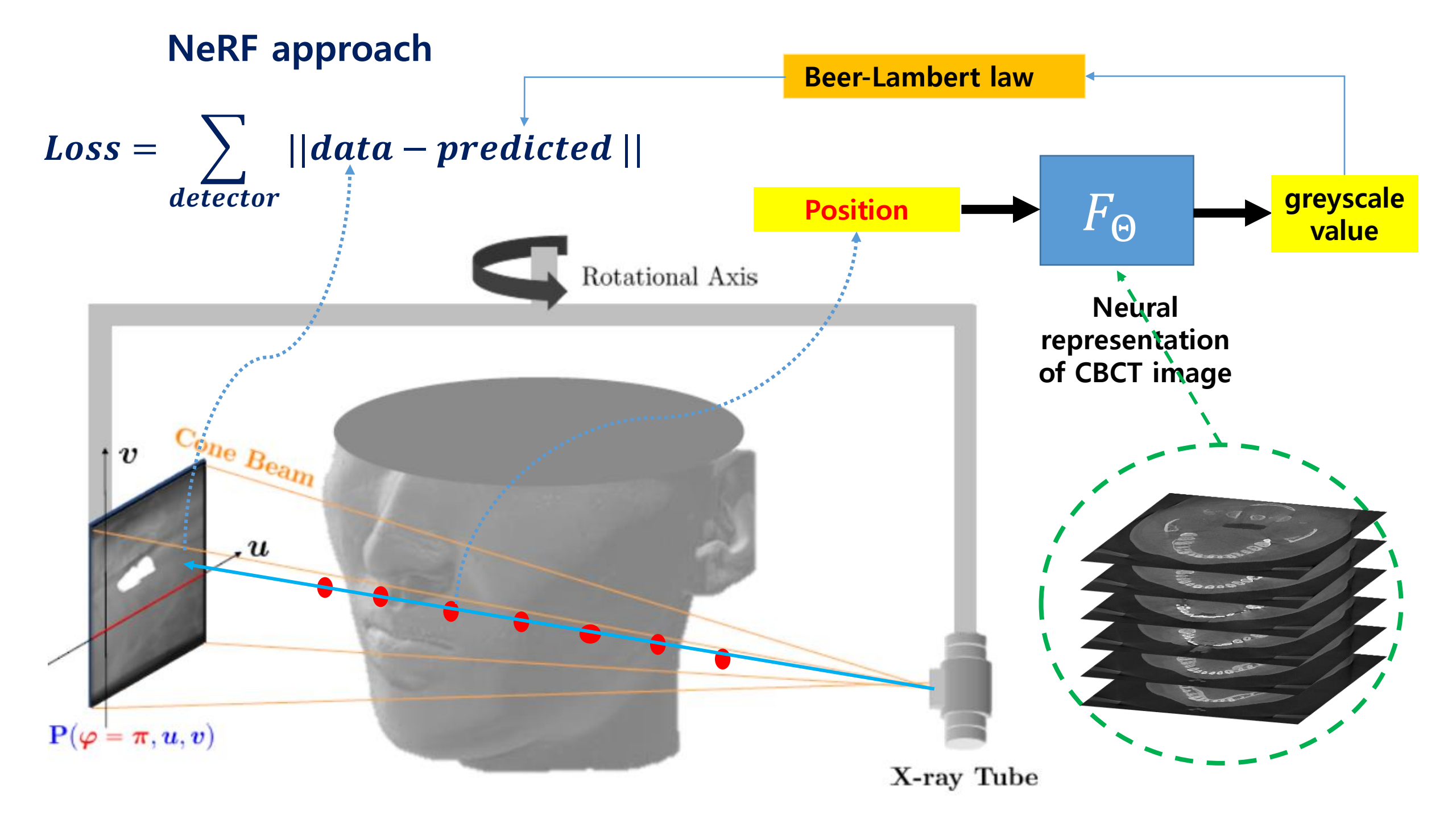
HS PARK, KW JEON, SH LEE, JK SEO (IEEE Access 2022)

Comments

- It is crucial to incorporate a strong image prior that constrains the relationships between pixels based on underlying head anatomy.
- While regularization techniques are commonly used for this purpose,
 they have limited performance as they lack global controls between pixels.

Neural Representation

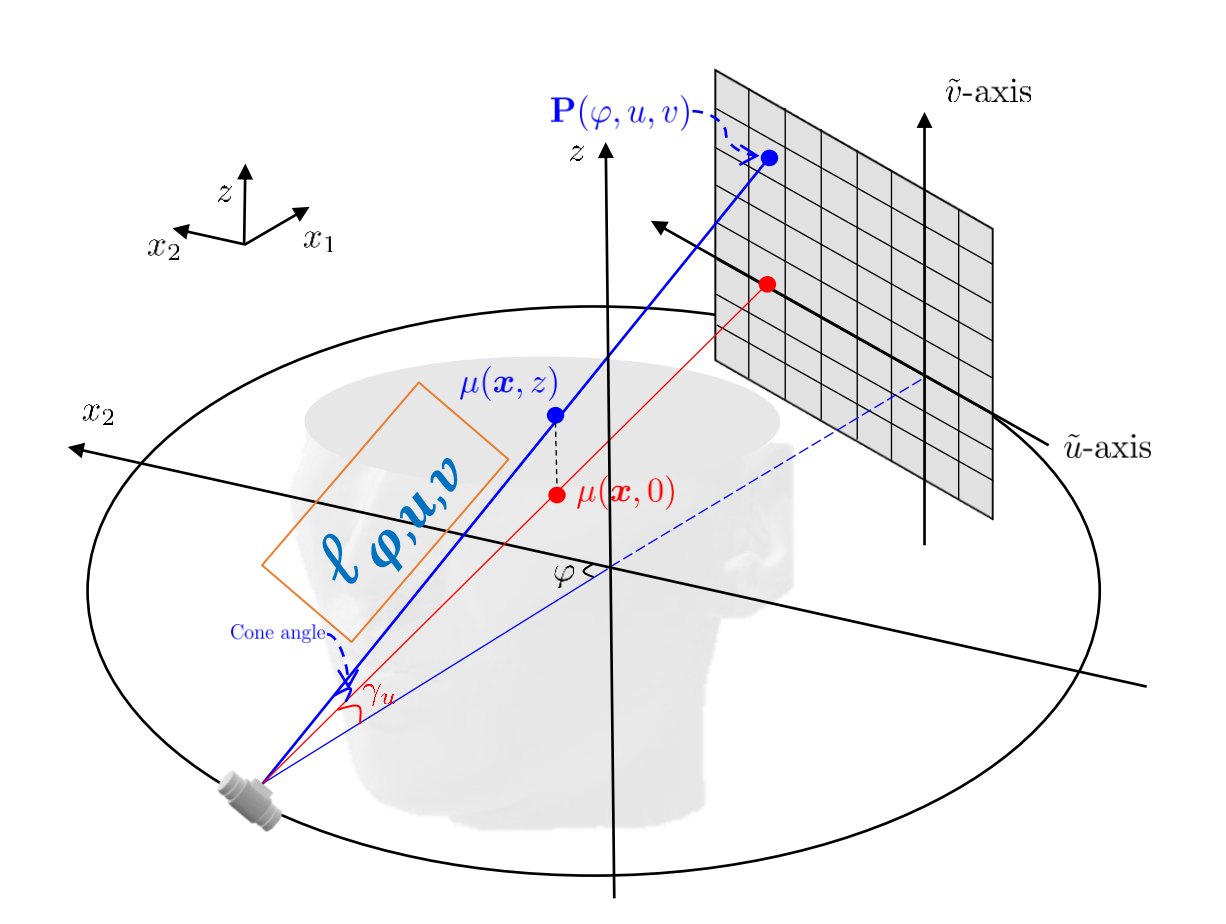
Warning: Please note that this approach is currently at an early stage of development, with most of the testing being performed using phantom experiments rather than real-world experiments.



About the predicted data

Projection Data: Beer-Lambert law

$$P_{compute}(\varphi, u, v) = -\ln \int \eta(E) \exp \left(-\int_{\ell_{\varphi,u,v}} \mu_{E}(x, y, z) ds\right) dE$$



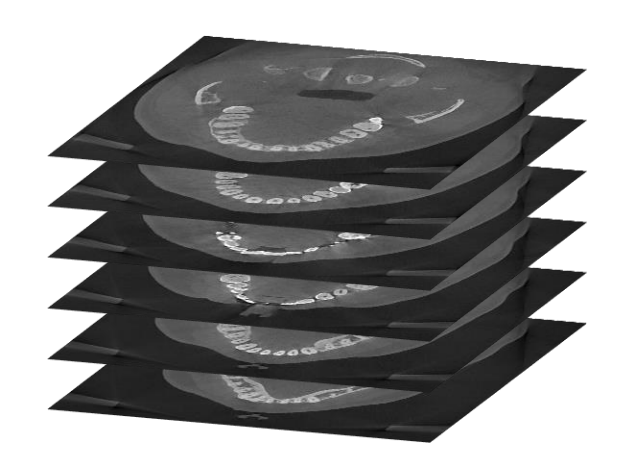
$$=G[\mu_{E_0},\sigma](\varphi,u,v)$$

 σ is determined by $\eta(E)$ and $\frac{\partial \mu_E}{\partial E}\big|_{E_0}$

CT image representation

Pixel or voxel-based representation

$$\mu = \underset{\mu \in R^{\#voxels}}{argmin} ||A\mu - P|| + Reg(\mu)$$



unknowns=# voxels ($512 \times 512 \times 300$)

The vast dimension of the solution space and the inconsistent data necessitate the incorporation of an image prior that constrains the relationship between pixels based on the underlying head anatomy. Regularization techniques have limited performance due to their inability to provide global controls.

Neural representation

 $F: x \mapsto \mu(x)$



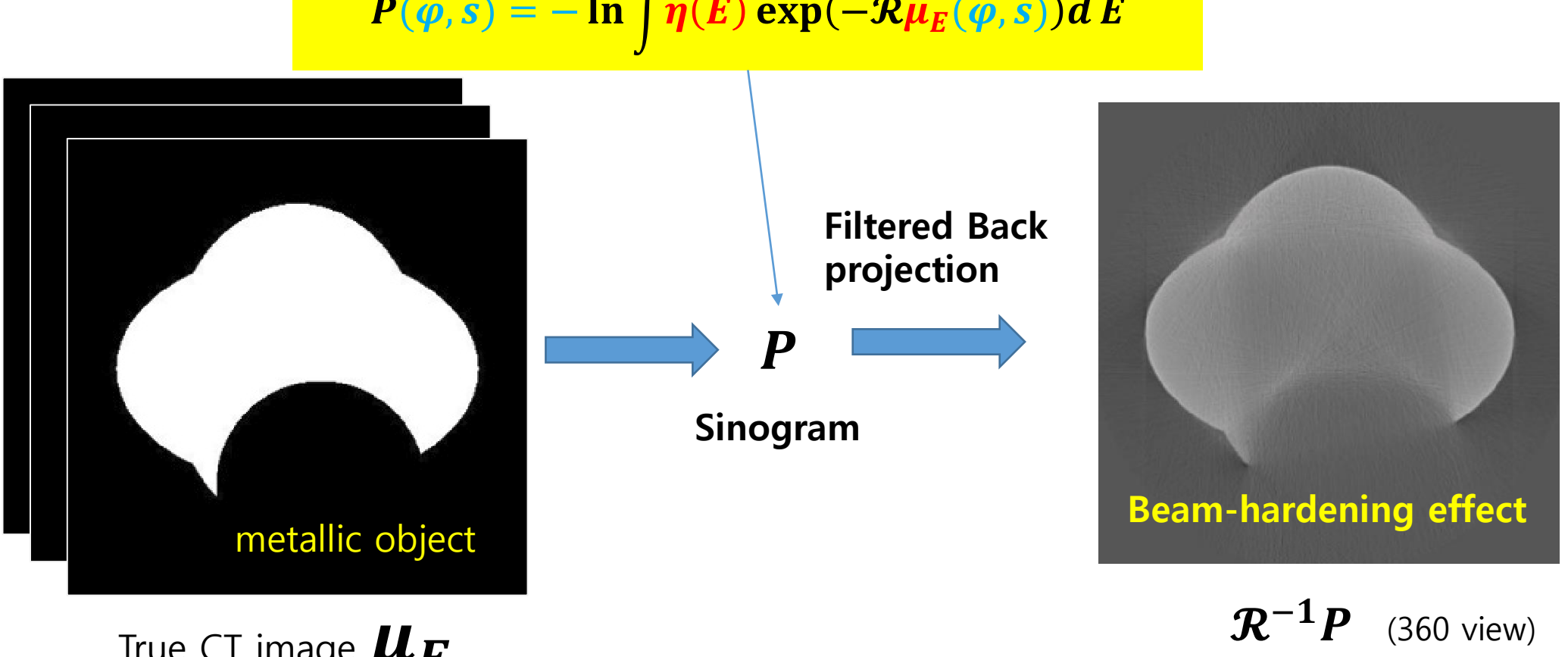
unknowns=# 0

The dimension of the solution space is small. This neural provides a "fully connected" solution, as each pixel is connected to every other pixel in the image.

Numerical experiments

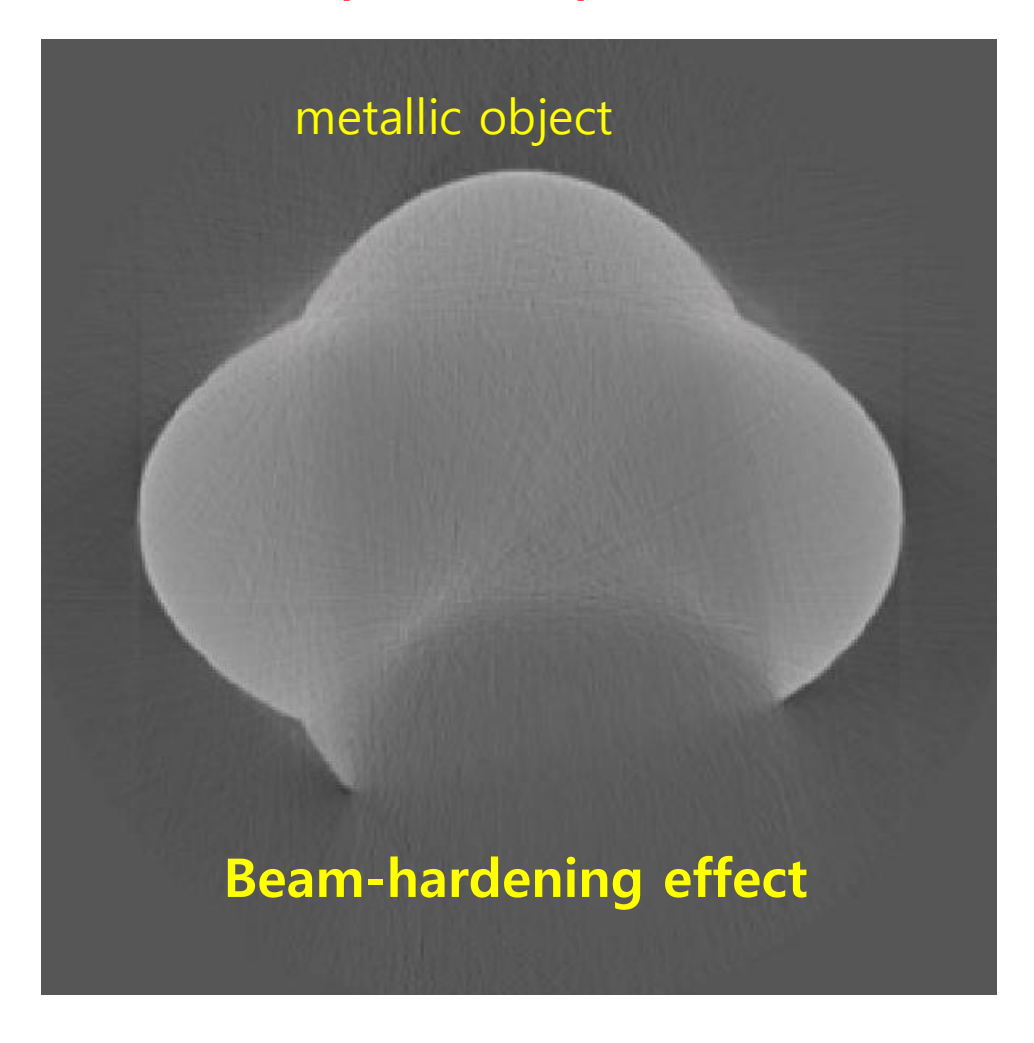
CT reconstruction of high-attenuation objects in a standard CT imaging environment

$$P(\varphi, s) = -\ln \int \eta(E) \exp(-\mathcal{R}\mu_E(\varphi, s)) dE$$

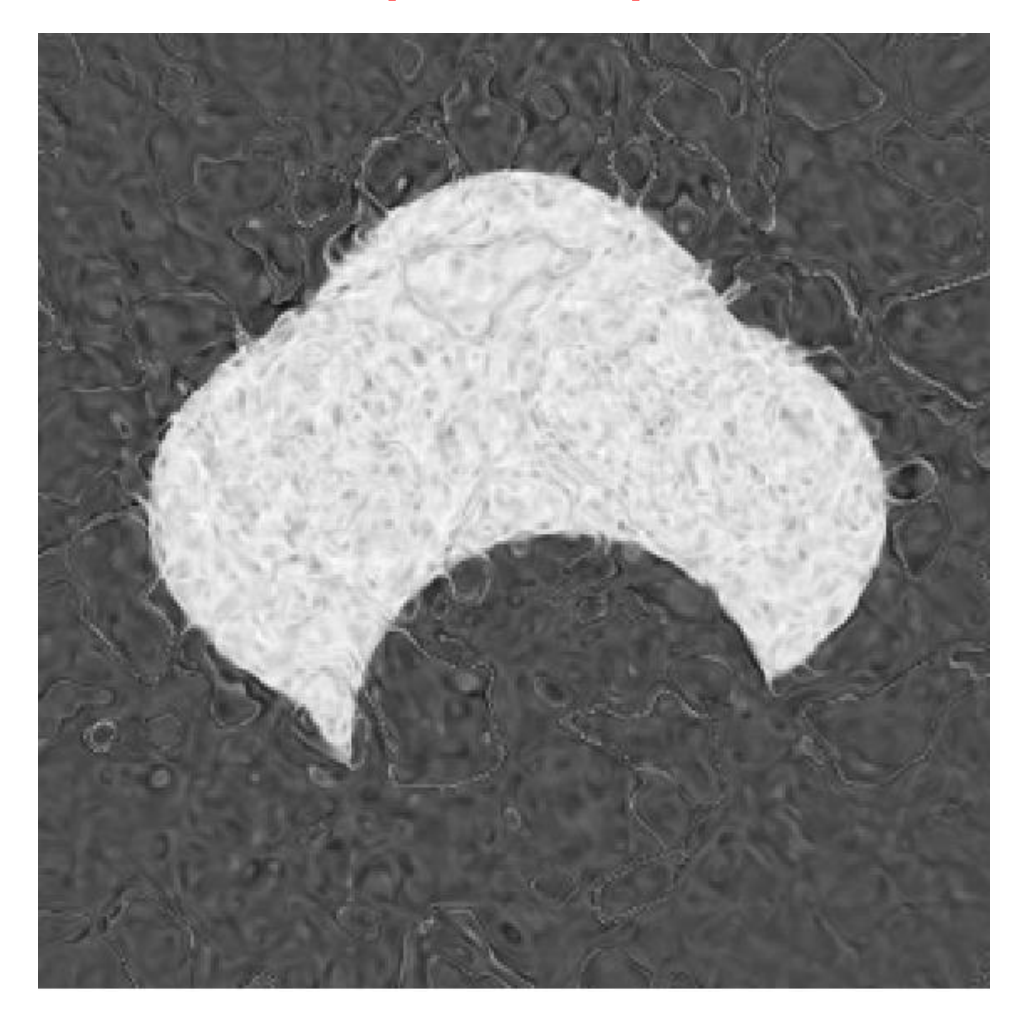


True CT image μ_E

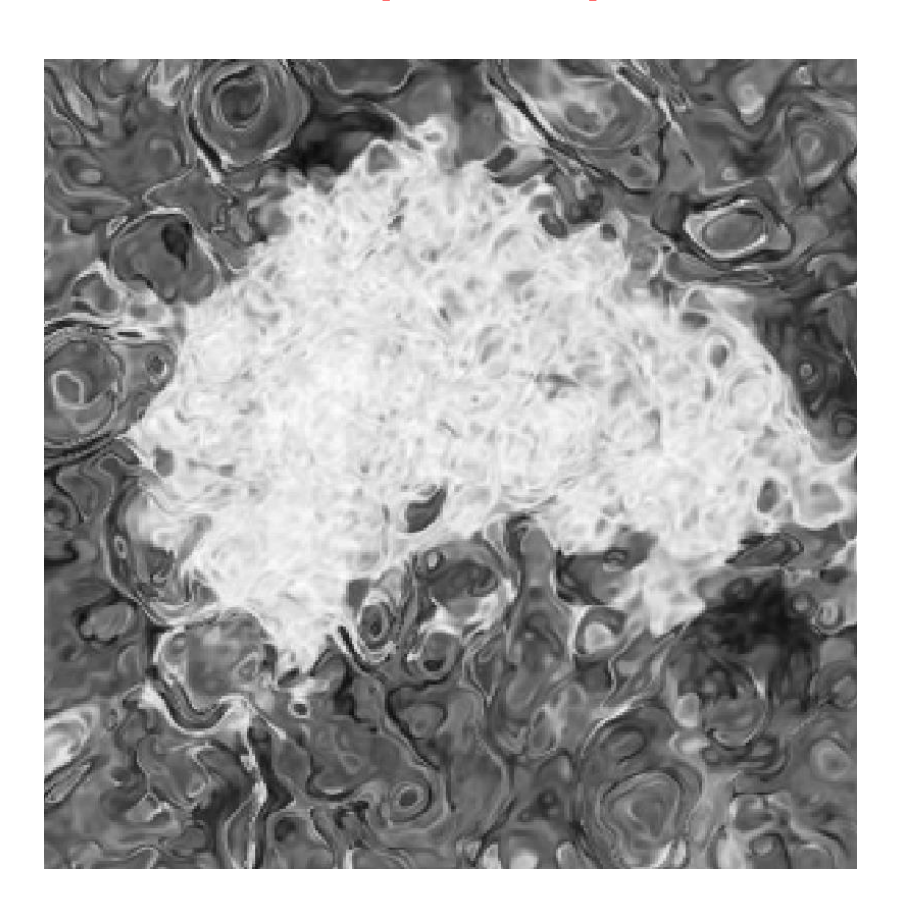
Reconstruction by FBP (360 view)



Reconstruction by NeRF (30 view)



Reconstruction by NeRF (5 view)



Reconstruction by NeRF (120 view)



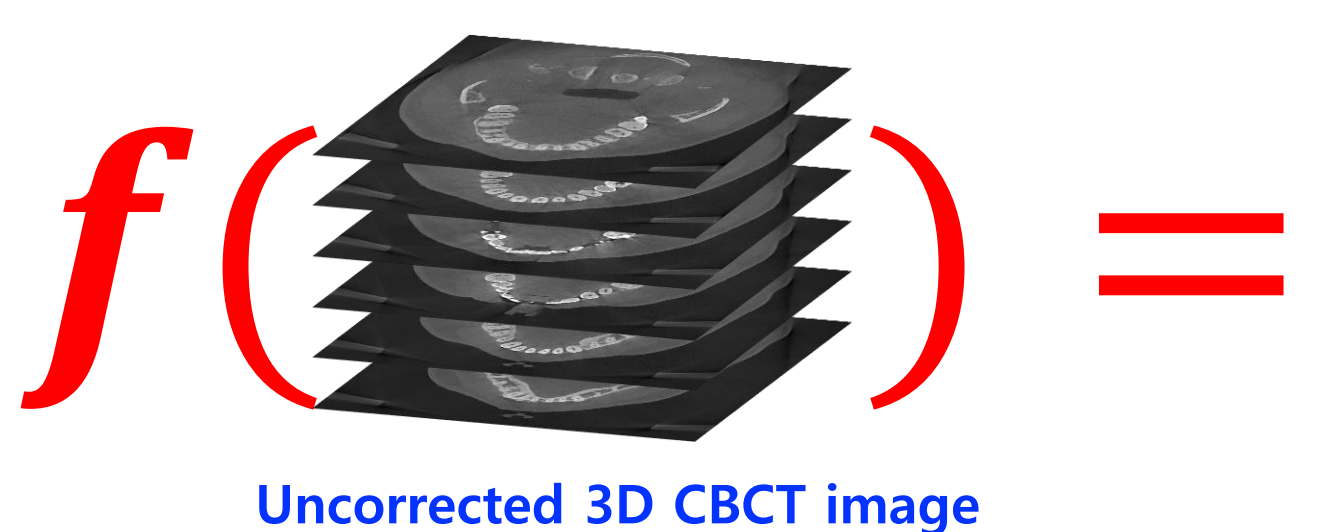
- Conventional CBCT reconstructions use a pixel or voxel-based approach to represent image, but this approach in low-dose dental CBCT can face challenges due to the large dimension of the solution space and inconsistent data in the presence of metal implants.
- Neural representations using MLPs utilize implicit representations that
 can capture complex relationships between image pixels more efficiently.
- These representations enable a significant reduction in the dimension of the solution space, (HOPE) making CBCT reconstruction with highly undersampled data more efficient.

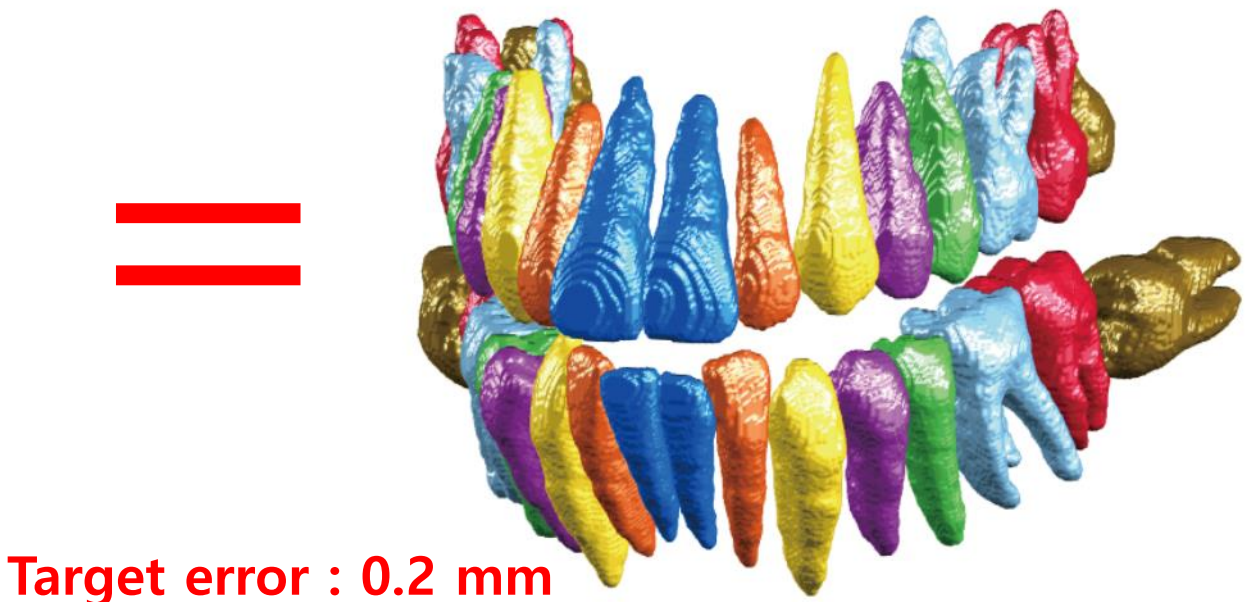
Develop a MAR method for Dentomaxillofacial imaging Giving up soft tissue details.

Main issue: 3D Teeth & Jaw Segmentation



Output: MAR & segmentation

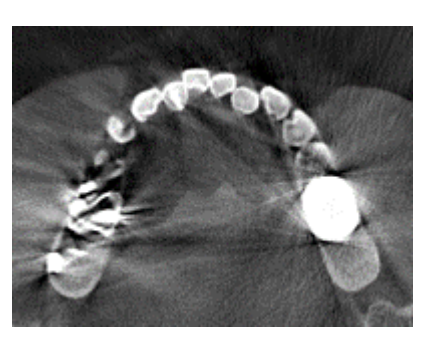




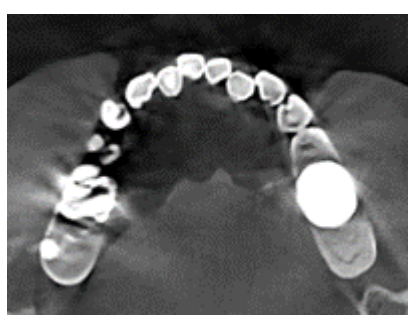
Without using a good image prior, it is difficult to get accurate segmentation due to the difficulty in handling metal-induced artifacts.



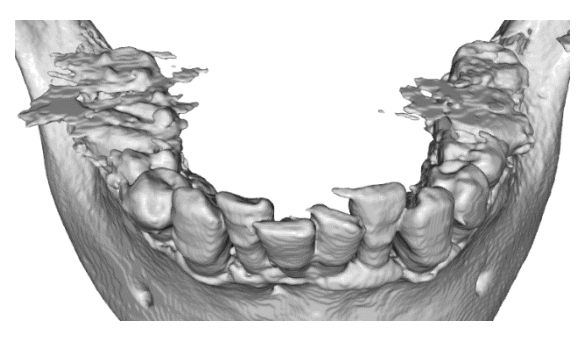
(a) Multiple gold dental prostheses



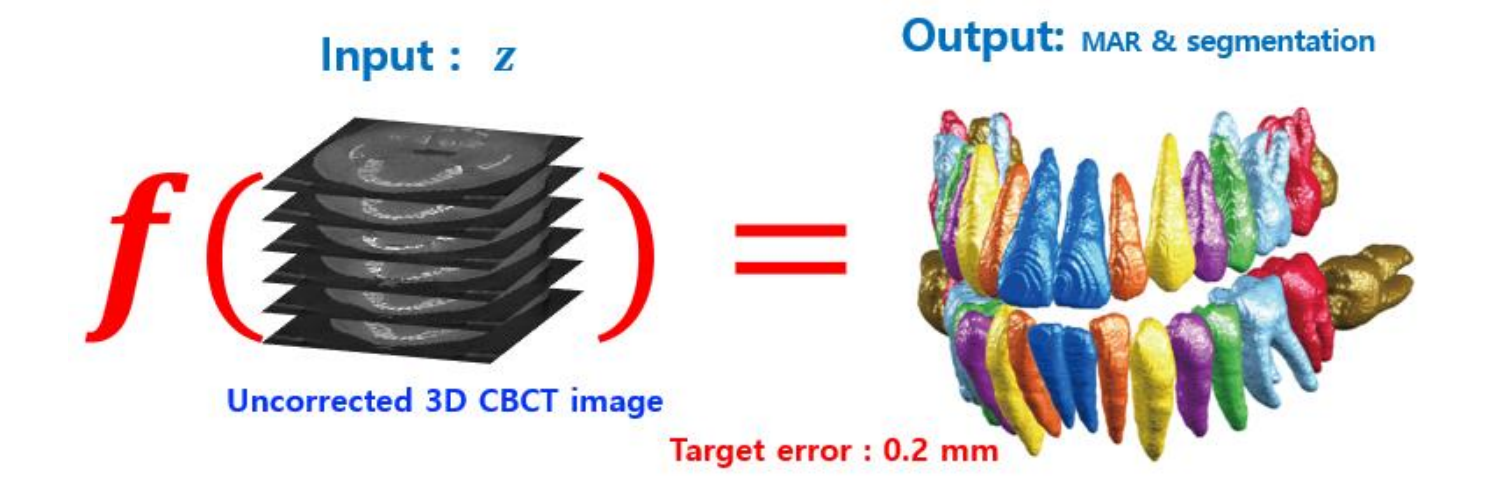
(b) CBCT before MAR



(c) CBCT after MAR



(d) Bone thresholding segmentation

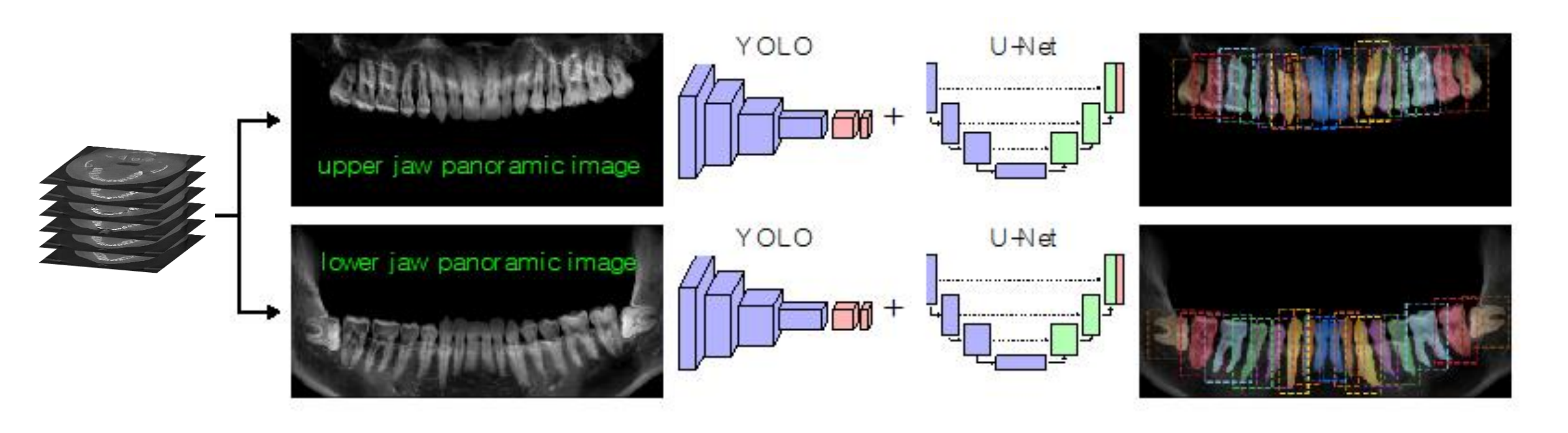


The key idea: Get a good prior knowledge that is obtained by generating a clean **panoramic image** from the noisy CBCT image.

The panoramic image is not much affected by metal-related artifacts. 2D shape of Mapping from CBCT tooth can be to panoramic image seen. CBCT image Panoramic image Dental arch This image was obtained by generation integrating along the normal direction of the dental arch. This integration cancels out metal **Metal-artifact** artifacts. contaminated image

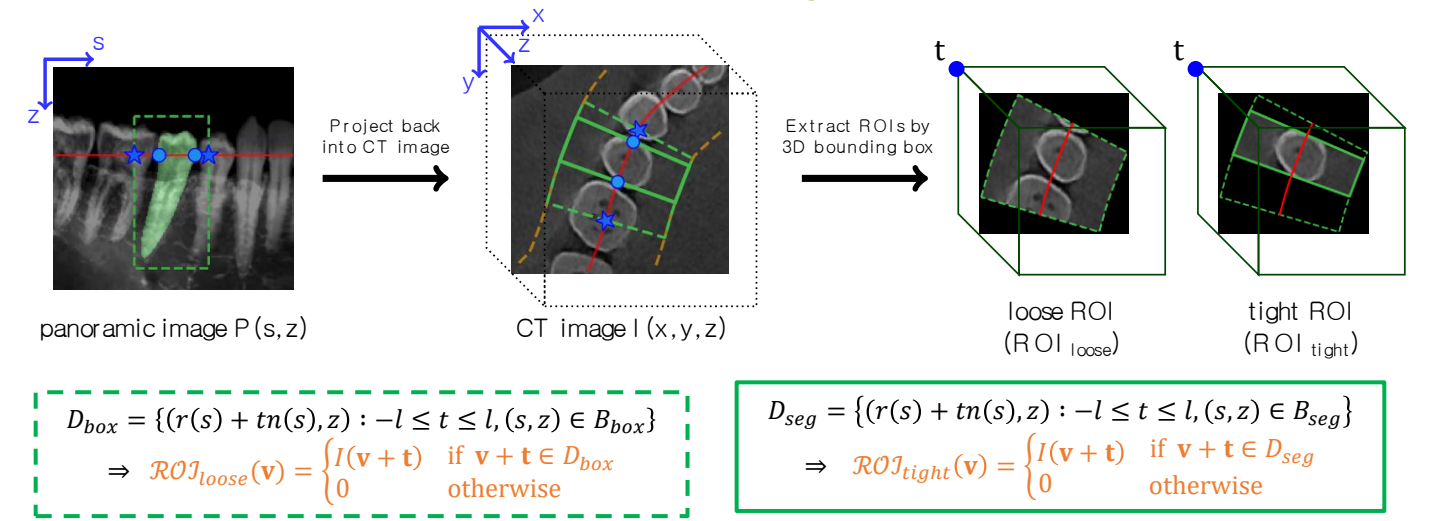
Accurate 2D tooth segmentation is obtained from panoramic images.

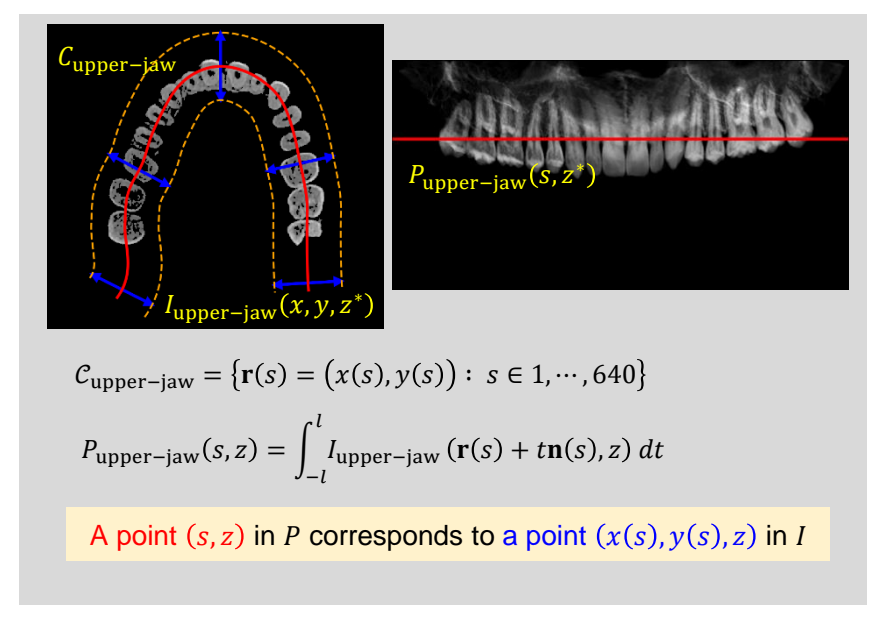
This 2D segmentation is used to find accurate 3D tooth ROIs.



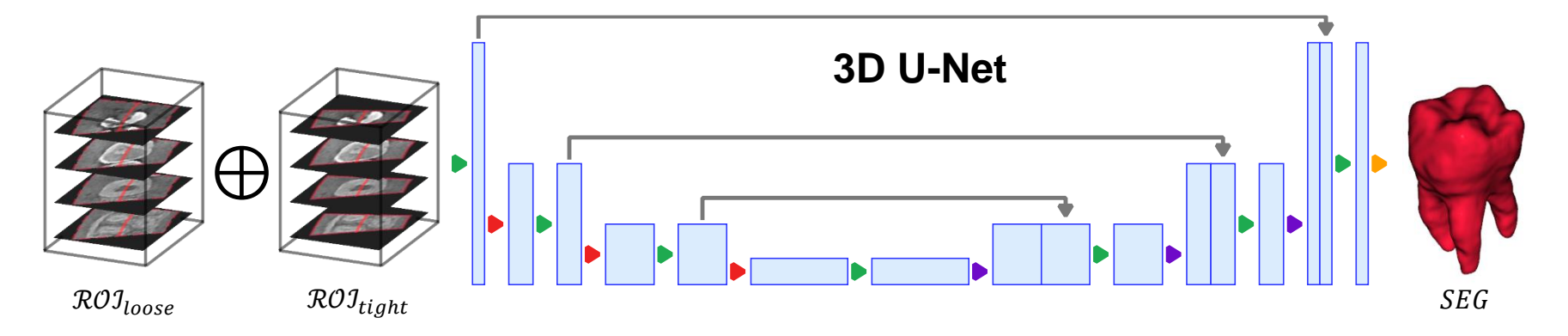
2D tooth segmentation provides a **deep learning friendly environment** for 3D tooth segmentation.



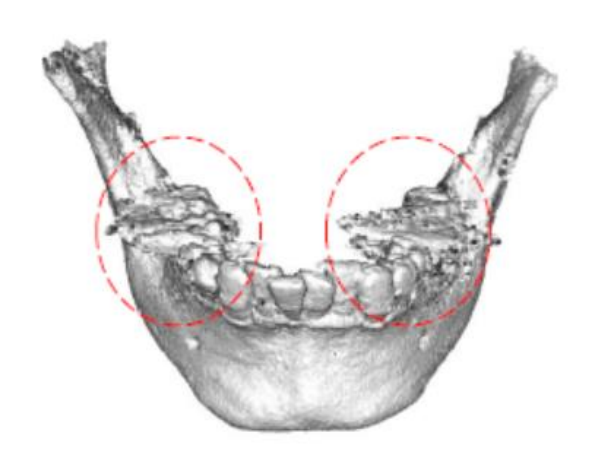


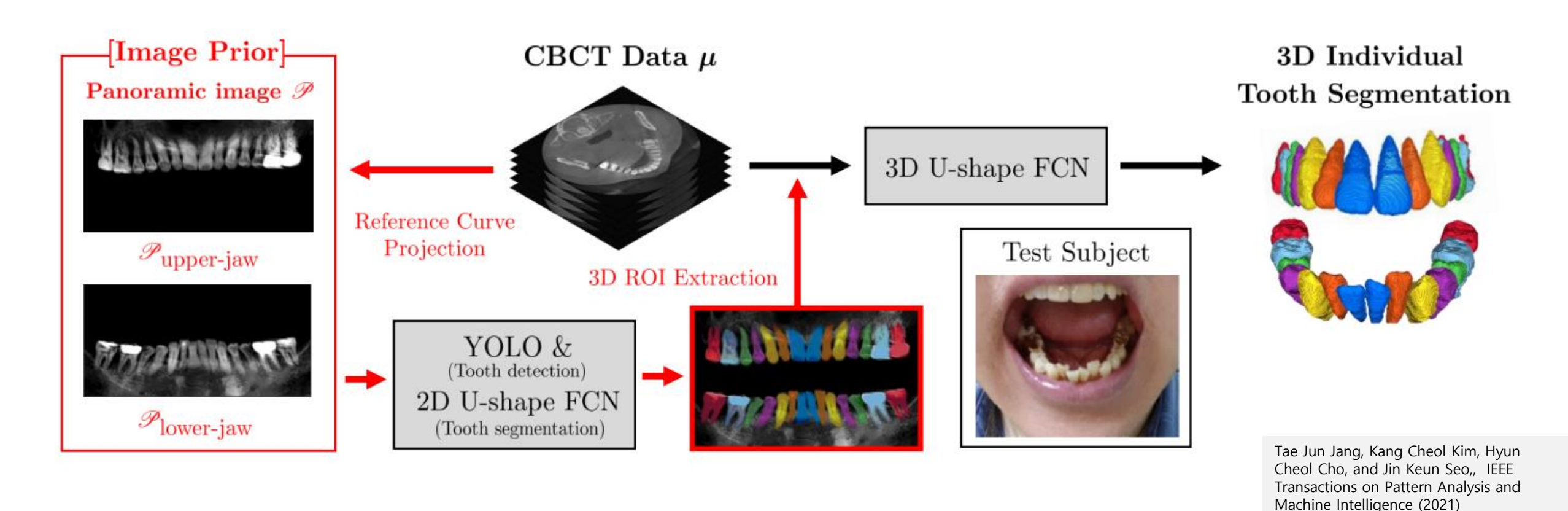


Individual tooth segmentation from the obtained loose & tight ROIs



Summery: The panoramic images generated by CBCT data can be excellent prior information for 3D tooth segmentation.



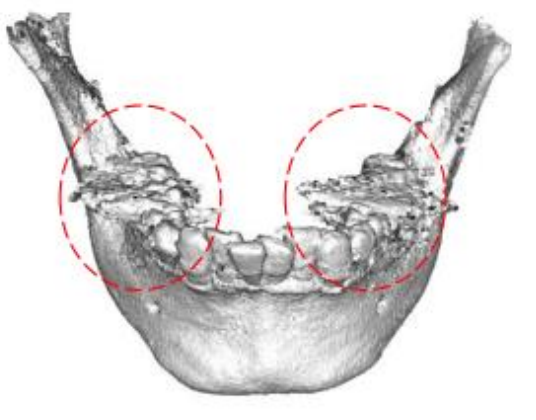


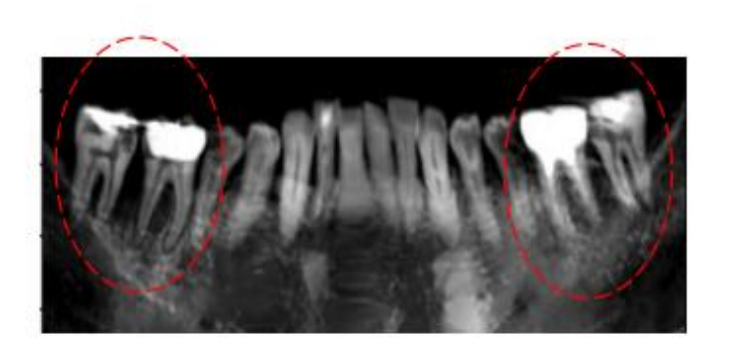
Although the aforementioned method using the panoramic image prior has achieved great success in accurate tooth segmentation, there is still a limit to accurately reconstructing teeth surfaces.

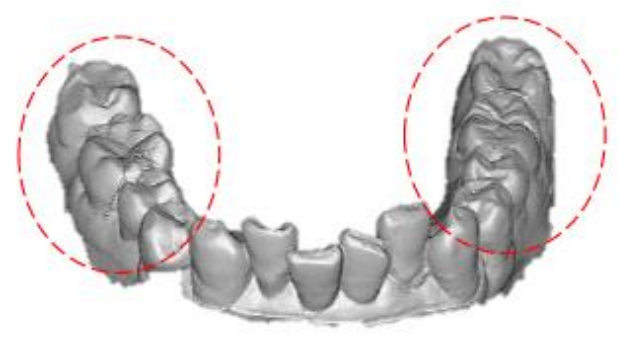
Concrete image prior: Intra-Oral Scan (IOS)

The IOS as a concrete image prior can be used without increasing X-ray dose exposure.









(a) Subject

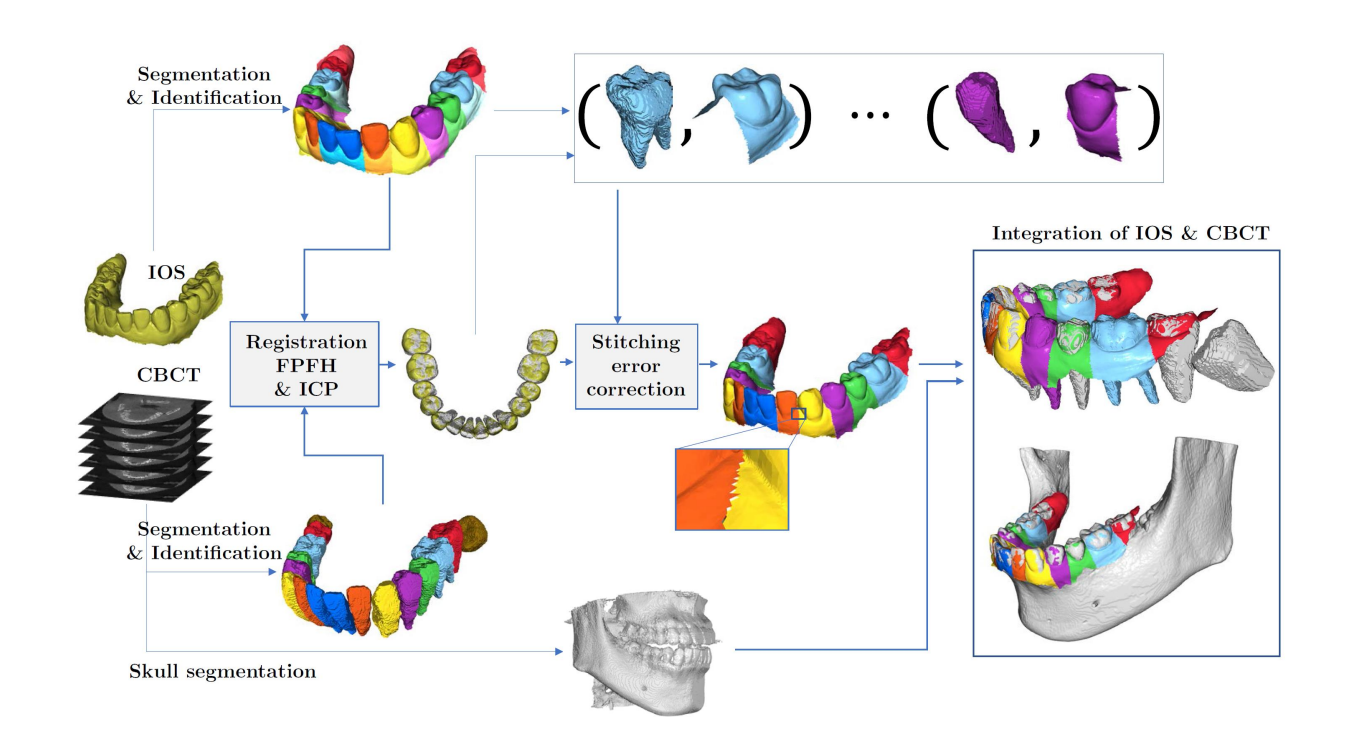
(b) CBCT

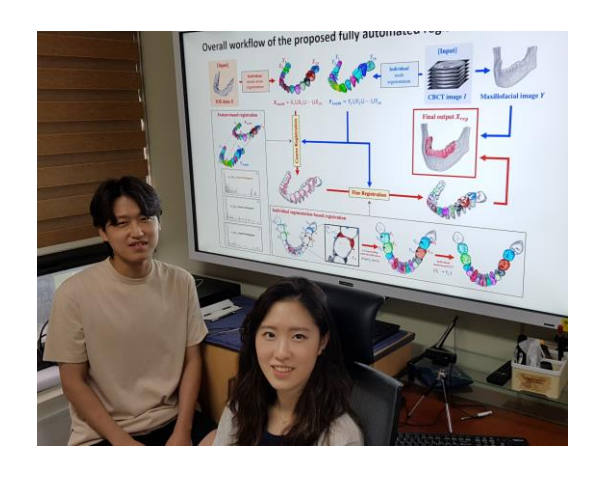
(c) Panoramic image

(d) Intra-oral scan

Fusion of CBCT and intraoral scan can eliminate

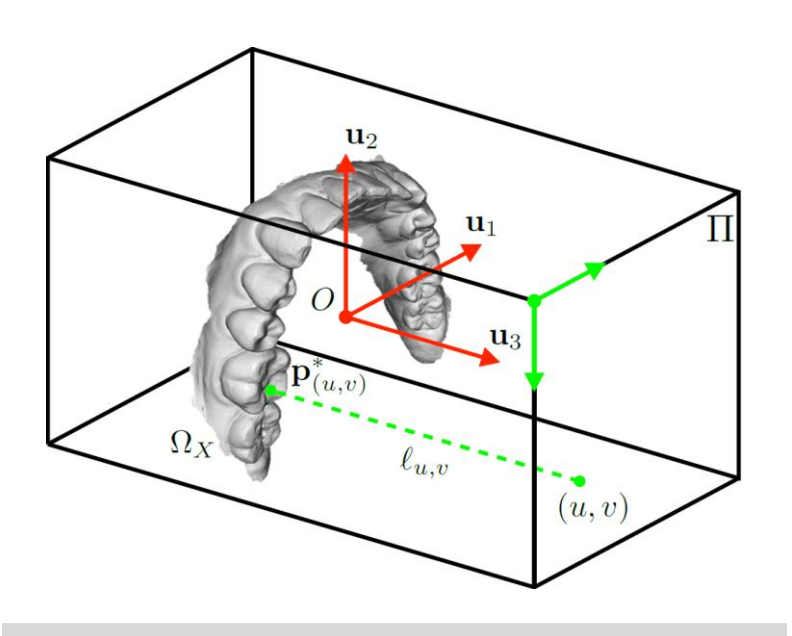
the cumbersome procedure of conventional impressions.





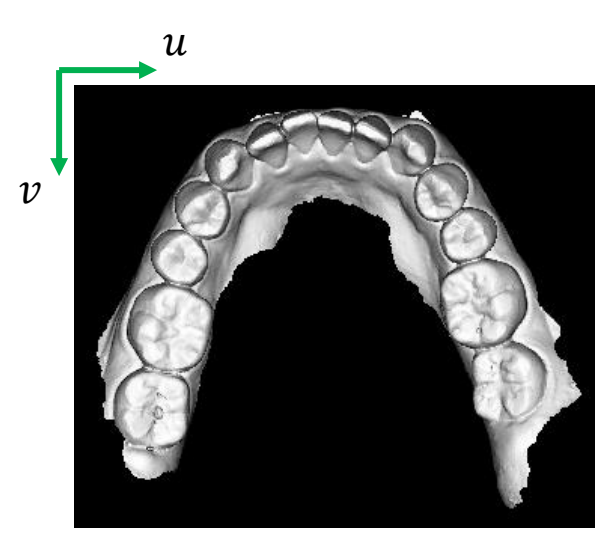
Jang T J, Yun H S and Seo J K 2022 Fully automatic integration of dental CBCT images and full-arch intraoral impressions with stitching error correction via individual tooth segmentation and identification arXiv:2112.01784

Step 1: Depth image generation

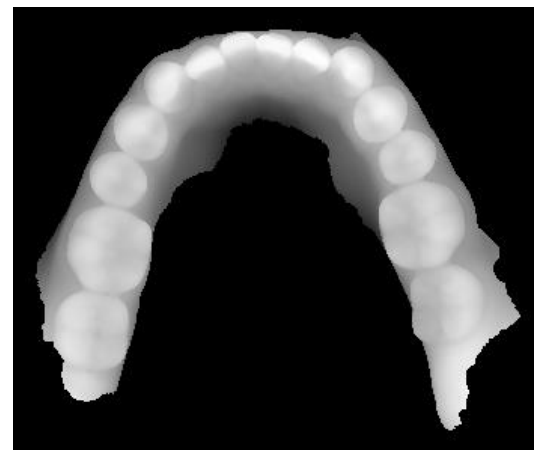


Orthographic Projection





Rendered image I_r



Depth image I_d

Using PCA, we align X in a new coordinate system with three axes
$$(\mathbf{u_1}, \mathbf{u_2}, \mathbf{u_3})$$
.

$$\tilde{X} = \begin{bmatrix} \mathbf{x}_1 - \bar{\mathbf{x}} \\ \vdots \\ \mathbf{x}_n - \bar{\mathbf{x}} \end{bmatrix}_{n \times 3} \mathbf{SVD} \Rightarrow V = [\mathbf{pc_1}, \mathbf{pc_2}, \mathbf{pc_3}]$$

$$\mathbf{u}_{2} = \begin{cases} \mathbf{pc}_{2} & \text{if } \left\langle \mathbf{pc}_{2}, \sum_{\mathbf{x} \in X} \frac{\mathbf{x} - \overline{\mathbf{x}}}{\|\mathbf{x} - \overline{\mathbf{x}}\|} \right\rangle \geq 0, \\ -\mathbf{pc}_{2} & \text{otherwise} \end{cases}$$

$$\mathbf{u}_3 = \begin{cases} \mathbf{pc}_3 & \text{if } \langle \mathbf{pc}_3, \sum_{\mathbf{x} \in X} \mathbf{n_x} \rangle \ge 0 \\ -\mathbf{pc}_3 & \text{otherwise} \end{cases}$$

$$\mathbf{u}_1 = \mathbf{u}_2 \times \mathbf{u}_3.$$

$$I_r(u,v) = \begin{cases} \max\left\{\left\langle \mathbf{n}_{\mathbf{p}_{u,v}^*}, \mathbf{u}_3\right\rangle, 0\right\} & \text{if } \ell_{u,v} \cap \Omega_X \neq \emptyset \\ 0 & \text{otherwise} \end{cases} \qquad I_d(u,v) = \begin{cases} 1 - \frac{\left\langle \mathbf{n}_{\mathbf{p}_{u,v}^*}, \mathbf{u}_3\right\rangle - z_{min}^*}{z_{max}^* - z_{min}^*} & \text{if } \ell_{u,v} \cap \Omega_X \neq \emptyset \\ 0 & \text{otherwise} \end{cases}$$

 $\ell_{u,v}$: a line passing through (u,v) with the direction \mathbf{u}_3 $\mathbf{n}_{\mathbf{p}}$: a unit normal at \mathbf{p}

$$\mathbf{p}_{u,v}^* = \operatorname{argmax} \{ \langle \mathbf{p}, \mathbf{u}_3 \rangle : \mathbf{p} \in \ell_{u,v} \cap \Omega_X \}$$

$$z_{max}^* = \max \{ \langle \mathbf{p}_{u,v}^*, \mathbf{u}_3 \rangle \}$$

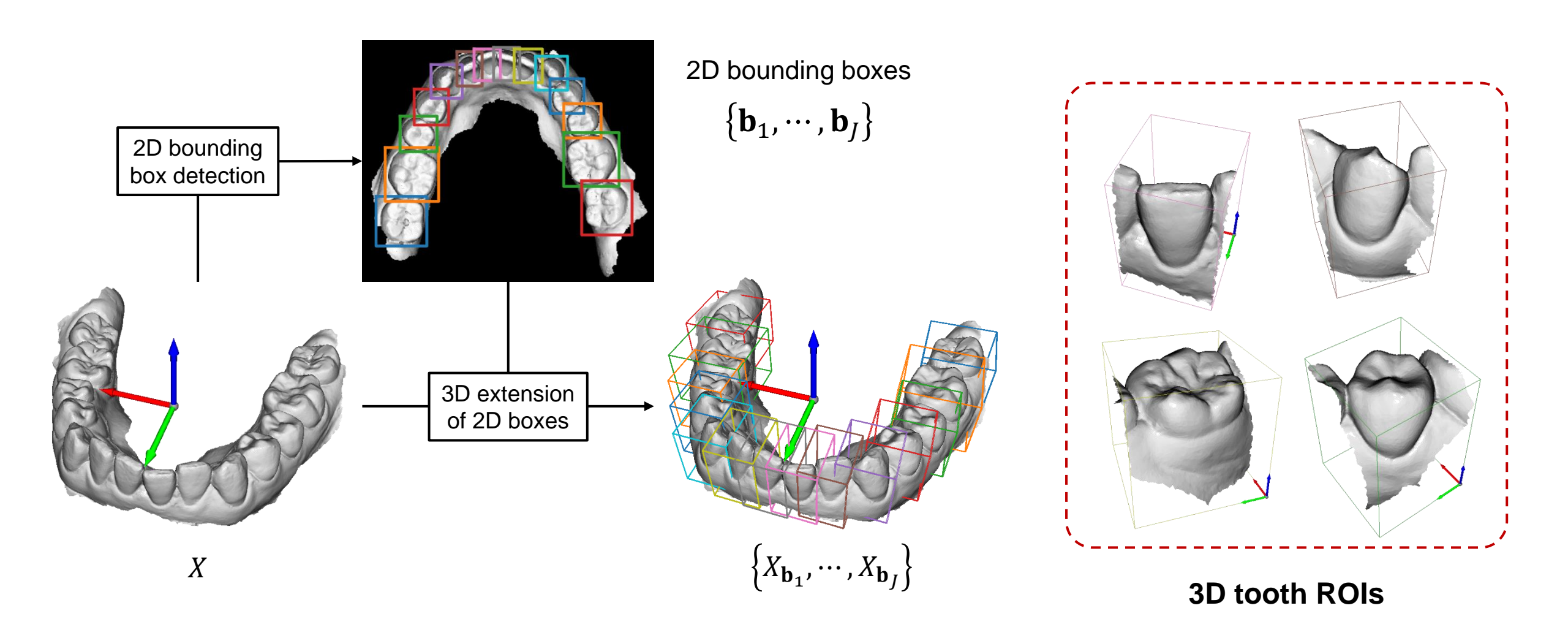
$$z_{min}^* = \min \{ \langle \mathbf{p}_{u,v}^*, \mathbf{u}_3 \rangle \}$$

$$z_{max}^* = \max\{\langle \mathbf{p}_{u,v}^*, \mathbf{u}_3 \rangle\}$$

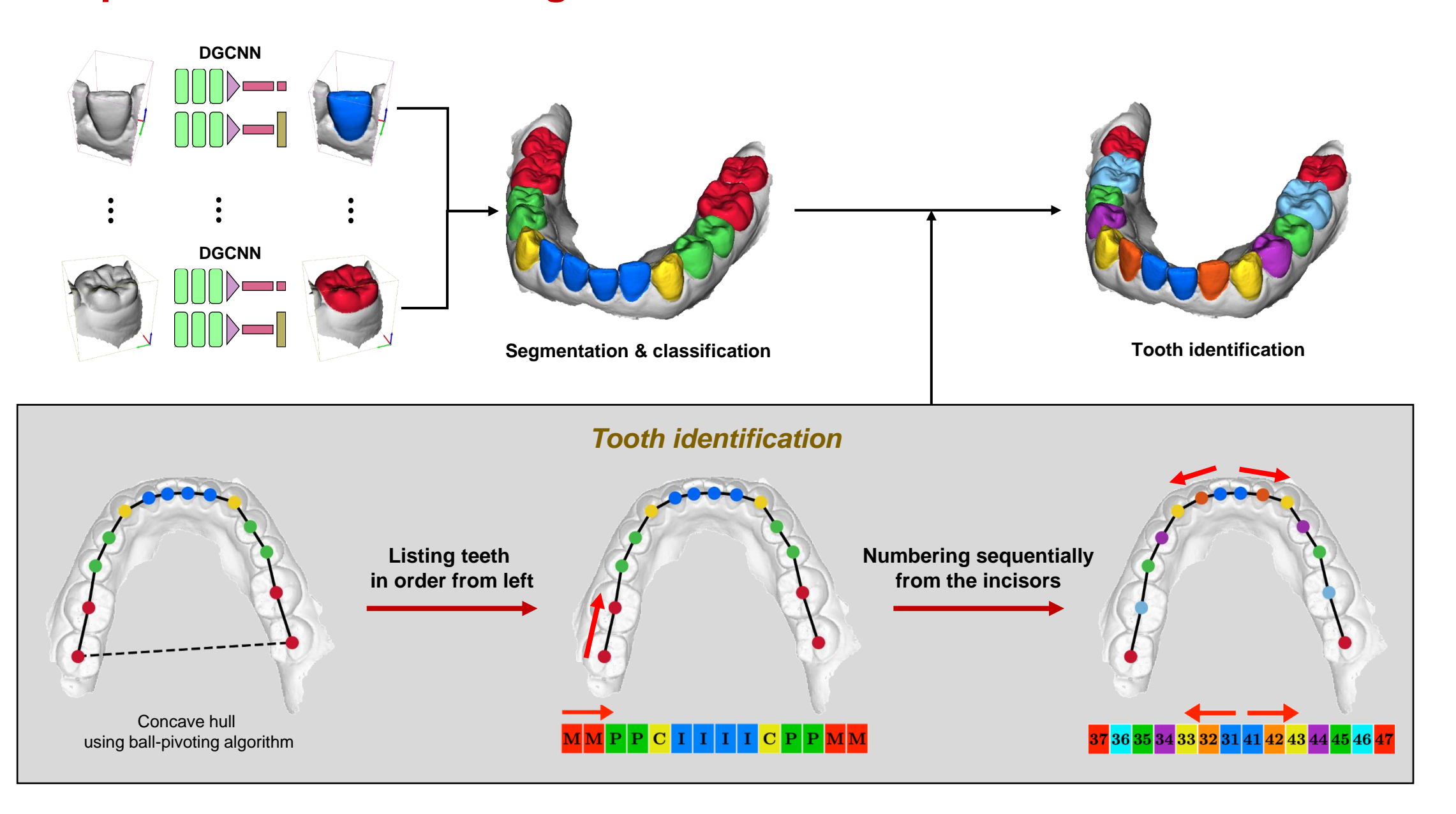
$$z_{min}^* = \min\{\langle \mathbf{p}_{u,v}^*, \mathbf{u}_3 \rangle\}$$

- The rendered image contains clear geometric features by lighting and shading the surface
- The depth image provides the tooth reliability by expressing the relative distance because the tooth positions protrudes forward than the gingiva and other tissues.

Step 2: tooth bounding box detection & 3D ROI extraction

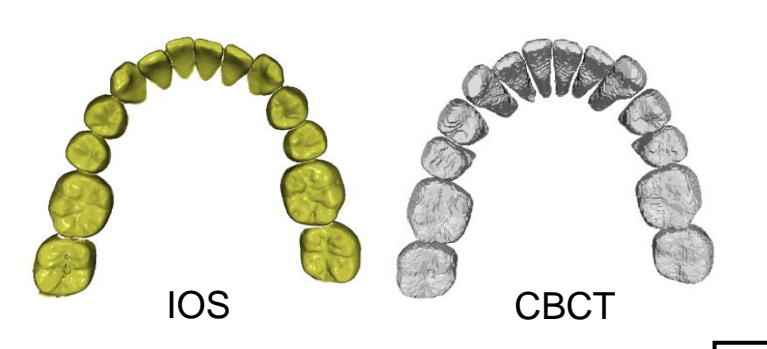


Step 3: Individual tooth segmentation and identification from the ROIs



Step 4: Global-to-local registration of IOS and CBCT

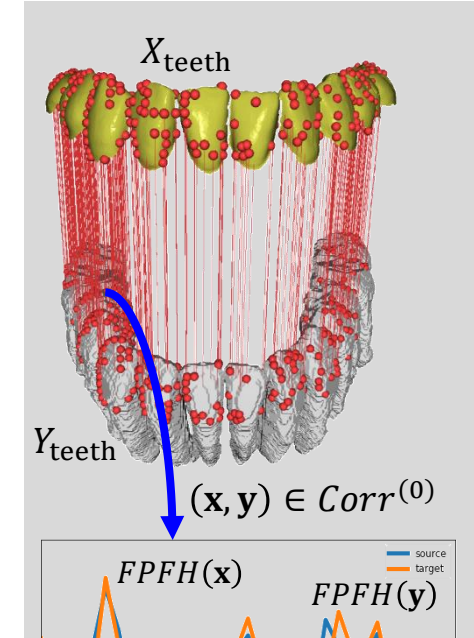
Two stage registration: 1) FPFH (Fast point feature histogram) for global initial alignment
2) ICP(Iterative Closest Point) for local refinement.



Rigid transformation

$$\mathcal{T}^* \coloneqq \mathcal{T}^{(K)} \circ \cdots \circ \mathcal{T}^{(0)}$$





Global initialization

FPFH(x) represents the **geometric features** at x, and the **relevant information** considering its neighboring points.

$$\operatorname{match}_{Y_{\operatorname{teeth}}}^{FPFH}(\mathbf{x}) \coloneqq \underset{\mathbf{y} \in Y_{\operatorname{teeth}}}{\operatorname{argmin}} \|FPFH(\mathbf{x}) - FPFH(\mathbf{y})\|$$

$$Corr = \left\{ \left(\mathbf{x}, \mathsf{match}_{Y_{\mathsf{teeth}}}^{FPFH}(\mathbf{x}) \right) : \mathbf{x} \in X \right\} \cap \left\{ \left(\mathsf{match}_{X_{\mathsf{teeth}}}^{FPFH}(\mathbf{y}), \mathbf{y} \right) : \mathbf{y} \in Y \right\}$$

We sample randomly three pairs (x_1, y_1) , (x_2, y_2) , (x_3, y_3) , and select the m if the following condition is met:

$$\tau < \frac{\|x_i - x_j\|}{\|y_i - y_i\|} < \frac{1}{\tau}, \quad for \ i \le 1 < j \le 3.$$

We denote this filtered subset as $Corr^{(0)}$.

$$\mathcal{T}^{(0)} = \underset{\mathcal{T} \in SE(3)}{\operatorname{argmin}} \sum_{(\mathbf{x}, \mathbf{y}) \in Corr^{(0)}} ||\mathbf{y} - \mathcal{T}(\mathbf{x})||^{2}$$

Local refinement

T-ICP finds correspondences in two teeth with the same code.

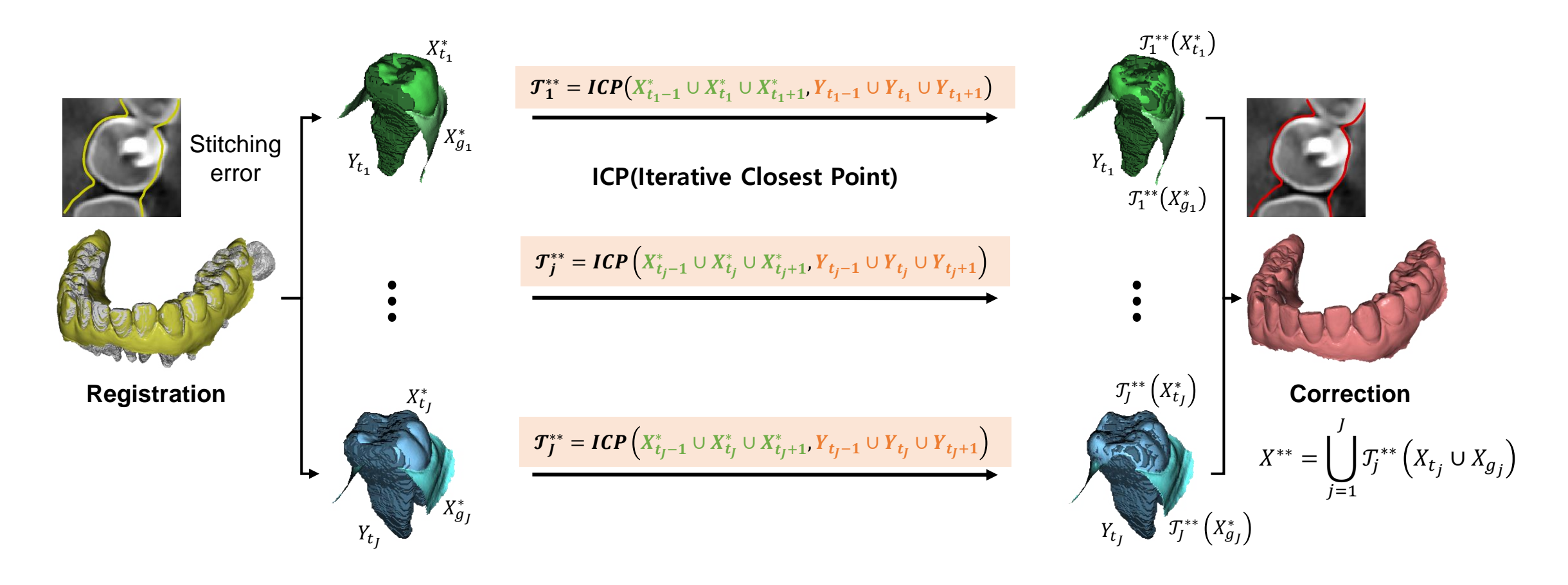
It prevents undesired point matching between different teeth.

$$Match_{Y_{teeth}}(\mathbf{x}) \coloneqq \underset{\mathbf{y} \in Y_{teeth}}{\operatorname{argmin}} \|\mathbf{x} - \mathbf{y}\|$$

$$Corr^{(k)} = \bigcup_{j=1}^{J} \left\{ (\mathbf{x}, \operatorname{match}_{Y_{t_j}}(\mathbf{x})) : x \in X_{t_j}^{(k-1)} \right\}$$

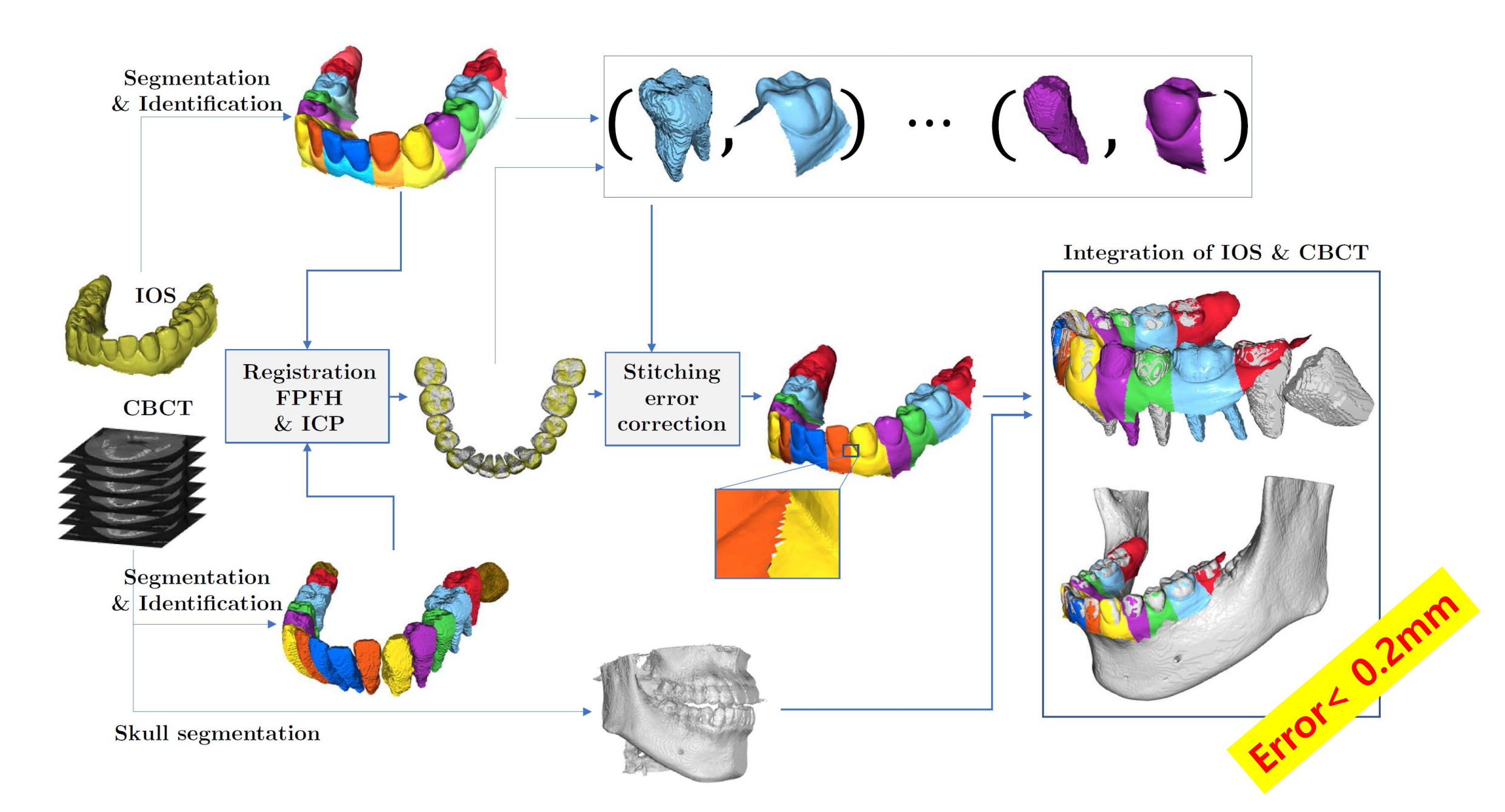
$$\mathcal{T}^{(k)} = \underset{\mathcal{T} \in SE(3)}{\operatorname{argmin}} \sum_{(\mathbf{x}, \mathbf{y}) \in Corr^{(k)}} ||\mathbf{y} - \mathcal{T}(\mathbf{x})||^{2}$$

Step 5: Stitching Error Correction in IOS

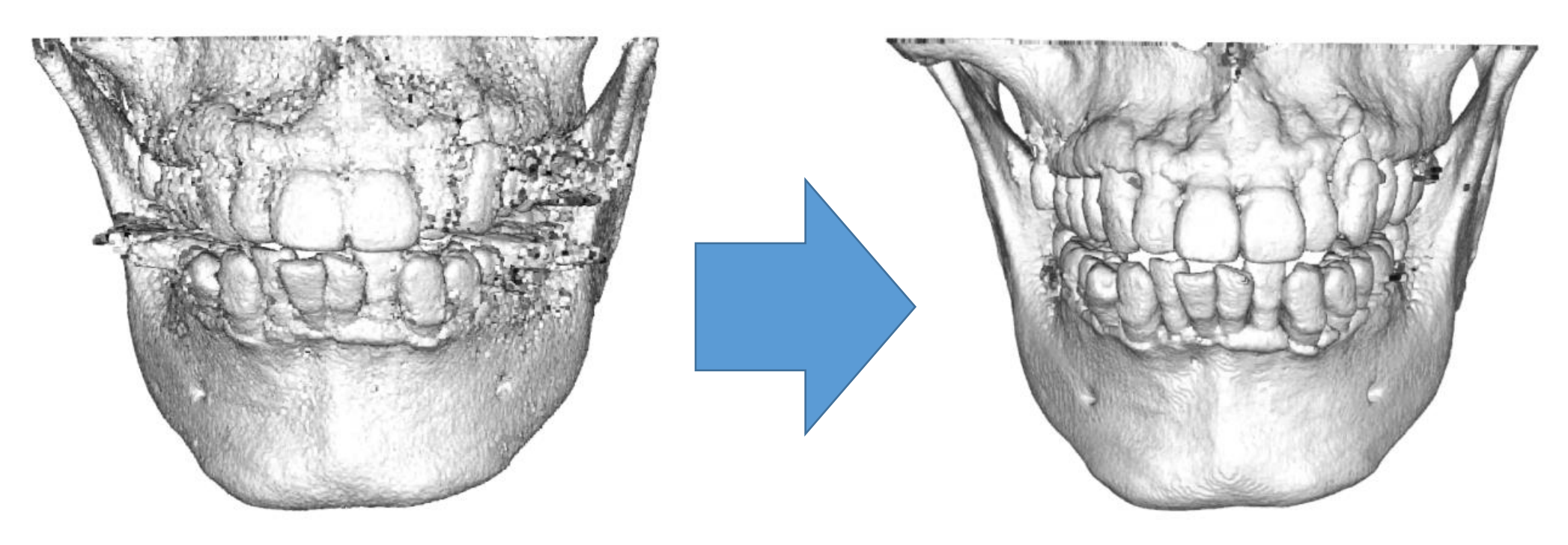


- By **referring to the CBCT teeth**, we edit the IOS models with the stitching errors.
- We use one tooth and two adjacent teeth on both sides for reliable correction.
- It takes advantage of the **fact that narrow digital scanning is accurate**.

Fusion of CBCT and intraoral scans



Deep Learning-based 3D bone-teeth-jaw modeling using CBCT & Intra Oral Scanner



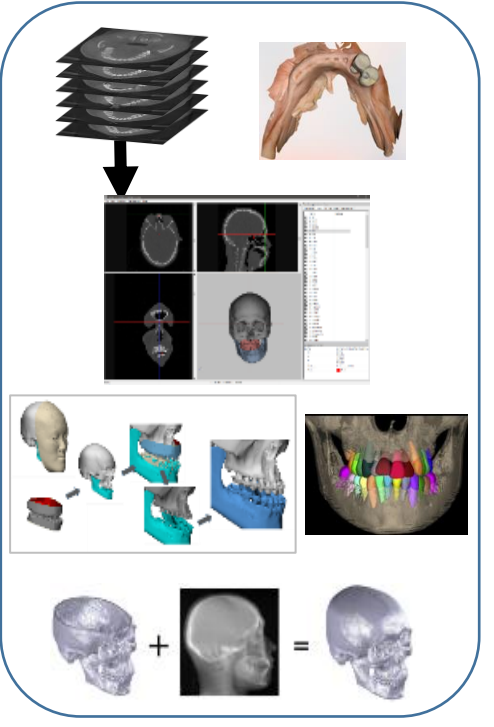
3D bone-teeth-jaw model generated from uncorrected CBCT image without using IOS.

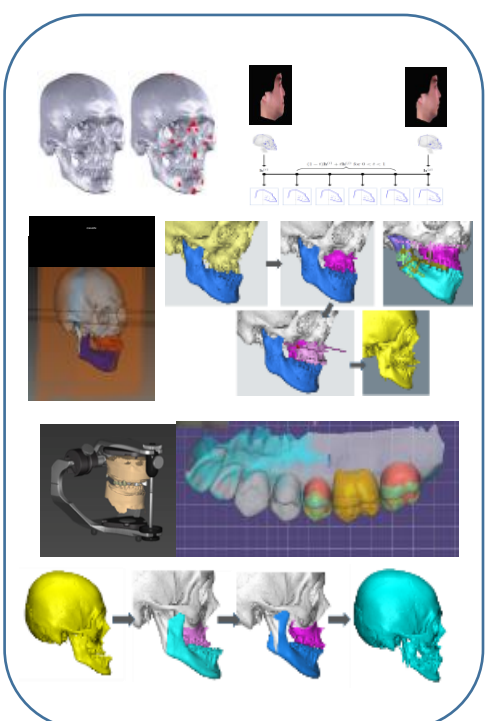
3D bone-teeth-jaw model obtained from the DL method that leverages **the tooth surface information from IOS.**

Thank you.

The aforementioned segmentation can be the core basis of Digital Dentistry.









Deep Learning and Medical Applications

